Supplementary Information

Table S4: Elevation of GCM grid cells for Puxian from PMIP2 GCMs
Table S5: LGM-Modern temperature differences at Puxian from PMIP2 GCMs
Table S6: LGM-Modern differences in hydrologic parameters from PMIP2 GCMs
Table S7: Calculated surface water $\delta^{18}O$ (i.e., precipitation $\delta^{18}O$) based on model of snail body water $\delta^{18}O$
Table S8: Hydrologic data used for snail body water model
Table S9: Comparison of LMDZ model output with other proxy records

A. Materials and Methods

A1. Sample description and preparation

32 modern terrestrial gastropod snail shells were collected from the Chinese loess plateau at Puxian in Shanxi Province (Fig. S1-S2; 36.421°N, 111.147°E, 1148 m). Modern snails were collected on the surface of the Loess Plateau. Individuals that recently died can be identified by the colorful organic coating (banding) on the shells. Specimens were identified as *Cathaica* sp. as shown in Fig. S2 and have an aragonitic mineralogy. Field observations show that snails are active only during the rainy season.

37 shells from the same site were selected from loess stratigraphic unit L1.LL1 which has been extensively described and is known to correspond to the Last Glacial Maximum (LGM) (1-3). The stratigraphic unit was identified by pedogenic observations in field and measurements of magnetic susceptibility. To obtain specimens of fossil snails and concretions, about 50 kg of loess sample was immersed in water until fully dispersed. Then the sample was passed through a 150-mesh sieve (150 μm) in the field. The >150 μm fraction that is dominated by authigenic grains, from which rhizoliths, carbonate concretion, pseudomycelia and fossil snail shells could be picked. Due to low abundance of snail shells, specimens were also hand picked from the LGM layer in the field. The resistance of snail shells to erosion compared to the loess matrix made snails quite obvious on the surface of the cliff. Previous work on shell preservation has indicated that shells of this age exhibit excellent preservation in the central Chinese loess, and that aragonite/calcite transformations are only seen in much older sediments(4). Soil carbonates were recovered from the same glacial loess strata at Puxian, and are typically brown nodules of less than 1cm diameter. The controls on the time of soil carbonate formation are purely stratigraphic at our site, however we note that sites proximal to ours coherent glacial-interglacial changes in soil carbonate isotopic composition have been observed(5), supporting the notion that these carbonates do in fact record information about the environment at the time their stratigraphic position suggests they should. The modern soil carbonate from the Badain Jaran Desert analyzed here, was a larger white nodule of greater than 2 cm diameter.

Individual gastropod shells were first cleaned with a course-grained paintbrush to remove large fragments of soil and or organic material. Shells were gently crushed to produce large fragments and then sonicated and washed 6-10 times in deionized water, a procedure that produced very clean shell material free from any macroscopic contaminants. Shell material was then dried at 50°C overnight, and then crushed into a fine powder with a pestle and mortar.

A2. Stable isotope analysis

Approximately 8-12 mg samples of calcium carbonate were reacted for 20 minutes on a 90°C online common phosphoric acid bath system described previously(6). CO_2 gas was immediately frozen by liquid nitrogen, after passing through a dry ice/ethanol trap. Cryogenic purification of CO_2 was achieved using an automated online vacuum line, as described previously(6). Additional automated sample cleanup steps included passing sample gas through a Porapak Q™ 120/80 mesh GC column at -20°C to remove potential organic contaminants and silver wool (Sigma-Aldrich) to remove sulfur compounds. $\delta^{13}C$, $\delta^{18}O$, Δ_{47}, and Δ_{48}, in CO_2 derived from the phosphoric acid digestion

of carbonates was determined using two different Thermo Scientific MAT 253 gas-source mass spectrometers at Caltech using published configuration and methods(6-8). Raw data and averages for each specimen data are reported in Tables S1-S3. Carbonate standards of know isotopic compositions were run every 4-5 analyses (Table S3).

In order to monitor cleaned CO_2 gas samples for the presence of contaminating molecules such as hydrocarbons and sulfur compounds at the important molecular masses Δ_{48} values were calculated in the same way as Δ_{47} values, by references to the Δ_{48} stochastic distribution as defined by the analysis of heated gases (7-9). Large deviations of over 1‰ from the Δ_{48} heated gas line are considered potentially indicative of the presence of contaminants and so these measurements are excluded from further analysis.

A3. Calculations to derive stable isotope values and their errors

Since the publication of the initial inorganic calibration of the carbonate clumped isotope thermometer(10), alternative calibrations based of experimental and theoretical data have been reported(11, 12). However, as the calibration line of Ghosh et al., 2006, appears to adhere most closely to most published calibration data derived from biologically precipitated calcite, aragonite, and apatite we will continue to use it in this study(13-15). These published biogenic calibration datasets do produce calibration lines with marginally different slopes and intercepts to the inorganic calibration of Ghosh et al., but these differences are small, particularly in the temperature range 20-35°C where most of the data in this study fall and the 95% confidence intervals over calibration lines overlap with each other(13). Ghosh et al. derived the following relationship between measured Δ_{47} values and carbonate growth temperature:

$$\Delta_{47} = 0.0592\ (10^6.T^{-2}) - 0.02$$

Where T is the temperature in Kelvin. As sample reactions were carried out at 90°C, rather than 25°C in Ghosh et al., 2006, we applied the empirically derived acid digestion fractionation correction of 0.08‰ for Δ_{47} values as reported by Passey et al., 2010 (6, 10), Errors in reported Δ_{47} values and calculated temperatures include the propagated uncertainty in heated gas determination and in sample measurement.

The vast majority of data for this study was collected before the proposition of an "absolute reference frame" for clumped isotope studies of CO_2 based on the analysis of water equilibrated CO_2 gases (16), We therefore present data in Table S1-S3 both relative to the stochastic value (i.e., the nomenclature used in most previous studies) and in the absolute reference frame. Data in the absolute reference frame are generated using an empirical transfer function developed using data for heated gases, an in-house Carrara Marble standard, and the vein calcite 102-GC-AZ01 using values in Table S3 following the procedure described in Dennis et al. (2011)(16). Nevertheless as no water equilibrated gases were analyzed we considered it most appropriate to continue to use the equations described in Ghosh et al., 2006 to convert our measurements into temperatures, as described above.

Average measured values on Mass Spectrometer 1 for Carrara Marble (n = 10) relative to the stochastic distribution are 0.366‰ and on Mass Spectrometer 2 (n = 7) are 0.348‰, whilst accepted values from our laboratory based on a large (>60) number of measurements are 0.352‰. Average measured values for Carrara Marble on both machines given in Table S3 on the absolute reference frame are 0.392‰, identical to the value of Dennis et al., 2011 (16) due to the nature of the transfer function used. For NBS-

19 average measured values on Mass Spectrometer 1 on the absolute reference frame was 0.382‰ (n=2) compared to an accepted value of 0.392‰. Relative to the stochastic distribution our measured value was 0.356‰ compared to an accepted value of 0.352‰. This standard was not run of Mass Spectrometer 2. 102-GC-AZ01 was run (n = 4) on Mass Spectrometer 2, yielding a value of 0.665‰ on the relative to the stochastic distribution, compared to an accepted value of 0.644‰. See Table S3 for original data.

For aragonite $\delta^{18}O$ calculations an acid digestion fractionation factor of 1.00854126 was used, calculated by extrapolation from a published calibration(11, 17). For calcite a value of 1.00821000 was used(18). Temperatures estimated using sample Δ_{47} values were used to calculate the $\delta^{18}O$ of water from which the mineral precipitated using paired measurements of carbonate $\delta^{18}O$ and the following published equations(17, 19).

$$1000 \ln \alpha(\text{Calcite-}H_2O) = (18.03.10^3)/T - 32.42$$

$$1000 \ln \alpha(\text{Aragonite-}H_2O) = (17.88.10^3)/T - 31.14$$

Propagated errors in water $\delta^{18}O$ and in Modern-LGM Δ_{47} temperature differences were calculated as follows:

$$E_{\delta 18Owater} = \sqrt{(E^2_{\delta 18Ocarbonate} + E^2_T)}‰$$

Where E is one standard error. To derive the E^2_T term for calculating the propagated error in $\delta^{18}O$, the uncertainty in the Δ_{47} derived temperature is converted into a per mil value using the appropriate equation.

Table S1 reports average stable isotope data for individuals and Table S2 reports individual analyses.

A4. PMIP2 simulations

In order to compare our proxy data to model results we utilized output from both ocean-atmosphere and ocean-atmosphere-vegetation coupled global circulation models (GCMs) from the PMIP2 (Paleoclimate Modeling Intercomparison Project, Phase II) database(20). Results from LGM and control simulations from the PMIP2 GCMs are reported in Figure 2 in the main text, Fig. S3 and Tables S4-S6. We acknowledge the international modeling groups participating in PMIP2 for providing their results for analysis, the Laboratoire des Sciences du Climat et de l'Environnement (LSCE) for collecting and archiving the model results. The PMIP 2 Data Archive is supported by CEA, CNRS and the Programme National d'Etude de la Dynamique du Climat (PNEDC). More information is available on http://pmip2.lsce.ipsl.fr/.

A5. Description of the high-resolution and standard-resolution simulations with the LMDZ model

The numerical simulations presented here were performed on the NEC-SX8 of the IDRIS/CNRS computer centre. This work represents the first time that a high-resolution simulation with isotopic diagnostics has been applied to LGM climate.

The LMDZ4 (Laboratoire de Météorologie Dynamique-Zoom) general circulation model (21) is the atmospheric component of the Institut Pierre-Simon Laplace coupled

model (IPSL-CM4) (22) used in CMIP3 (Coupled Model Intercomparison Project) (23). It is a grid point model. Water vapor and condensate are advected using a second order monotonic finite volume advection scheme(24, 25). The physical package includes the Emanuel convective scheme(26, 27) and a statistical cloud scheme(28). The isotopic version of LMDZ is described in detail elsewhere(29, 30).

The standard resolution of LMDZ is 2.5° in latitude, 3.75° in longitude and 19 vertical levels. The present-day (PD) simulation is forced by monthly-mean sea surface temperatures (SST) and sea ice calculated as the long-term average between 1979 and 2007 of the Atmospheric Model Intercomparison Project (AMIP)(30) SST and sea ice. The CO_2 concentration is set to 348 ppm. This simulation is very similar to the AMIP simulation forced by inter-annually varying SSTs described in detail in Risi et al., 2010(29). The isotopic composition of the precipitation and water vapor in the latter simulation has been comprehensively evaluated at daily, monthly and inter-annual time scales(29, 31-33).

The SST and sea ice forcing for the LGM simulation are based on simulations by a coupled model: IPSL-CM4(34, 35). The forcing is calculated by adding monthly-mean climatological LGM anomalies to the SST and sea ice forcing used in the PD simulation. The LGM anomalies are calculated as the difference between LGM and pre-industrial period simulated by the IPSL coupled model. Given the significant SST biases for PD in coupled models, this method allows us to use a simulation with realistic SSTs as a control simulation. To ensure that the SSTs are representative of a average climate, pre-industrial and LGM SSTs and sea-ice were averaged over 50 years. Greenhouse concentration, orbital setting and topography are set following PMIP2. The CO_2 concentration is set to 180 ppm. Orbital parameters are set following Berger, 1978(36). We use the ICE5G ice sheet reconstruction of Peltier, 1994(37). We increase the sea surface $\delta^{18}O$ by 1.2‰ compared to present day based on the reconstruction by Labeyrie et al., 1987(38). In one additional experiment, the LGM simulation was run with no ice-sheets, i.e. with present-day topography and land ice fraction.

Both PD and LGM simulations are run for 6 years and the 3 last years are analyzed. The isotopic composition from this LGM simulation has been evaluated against some ice-core, cellulose, groundwater and speleothem records throughout the globe in Risi et al., 2010(29). Whereas the $\delta^{18}O$ change in mid and high latitude was satisfactorily captured by LMDZ, the observed depletion observed at LGM in low latitude ice cores (Tibet and Andes) was systematically underestimated.

The specificity of the LMDZ model is to offer a zoom functionality to enable high-resolution simulation over a specific region. The grid can be stretched in such a way as to increase the resolution in a region of interest down to a few tens of kilometers, and decrease the resolution everywhere else. LMDZ can thus be used as a regional model. The major difference from a regional model is that the simulations remain global, so that the benefits of the high resolution on the large-scale circulation and the vapor isotopic composition can feedback on the global simulation. In mountainous regions such as the Andes(39) and the Tibetan region(32), it has been shown that the isotopic simulation is dramatically improved when using the zoom functionality. Based on the hypothesis that the difficulties of LMDZ to capture the depletion observed at LGM in low-latitude ice cores could be due to a coarse resolution(29), we thus performed zoomed simulations for the present day and LGM. This is the first time that a high-resolution simulation by an

isotopic model for a past climate is documented.

The zoom configuration used here is described in Gao et al., 2011(32). The resolution is about 50 km in a wide region from about 10°N to 50°N and 70°E to 120°E (Fig. S10). In the standard-resolution and zoomed simulations, the altitudes of the grid box containing Puxian are 833 m and 1117 m respectively. The zoomed simulation thus captures the actual altitude of Puxian (1148 m) much more accurately than the standard-resolution simulation. More generally, the topographic features of the Tibetan plateau and surrounding ranges are much better resolved (Fig. S10).

For numerical stability reasons in zoomed simulations, the winds need to be nudged (i.e. relaxed towards a prescribed state) outside the zoom. In Gao et al., 2011, winds were nudged towards re-analyses(32). Since there are no reanalysis for the LGM, we nudged the winds towards the 6-hourly wind fields simulated by the standard-resolution simulations described above. The relaxation time is 30 minutes outside the zoom and 6h inside the zoom. The longer time scale inside the zoom allows the model to create its own circulation resulting from the finely-resolved topography.

Our simulations are relatively short due to computational limitations. The standard-resolution simulations were run for 6 years and the last 3 years were analyzed. Year-to-year variability stem from intrinsic atmospheric variability only, since SST and sea-ice forcing's are monthly mean climatologies with no inter-annual variability. The standard deviations among the 3 analyzed years are 0.9K for temperature and 0.5‰ for precipitation $\delta^{18}O$ at Puxian in annual average. These values are lower than the LGM-PD differences discussed in this paper. In zoomed simulations, winds are nudged towards year 3 of the standard-resolution simulation during 3 years and the 2 last years were analyzed. The differences between the 2 last years are only 0.04K for temperature and 0.07‰ for precipitation $\delta^{18}O$ at Puxian in annual average, due to the nudging.

B. Analysis of results

B1. Systematics of clumped isotope thermometry in soil carbonates and terrestrial gastropods.

Pedogenic carbonates are thought to preferentially form in the warmer months, and so their stable isotope composition is thought to reflect environmental conditions during the summer months (eg. Breecker et al., 2009)(40). This idea was confirmed by a recent in depth calibration study of modern/recent soil carbonates of a range of morphologies, and from different multiple different localities (including China) showed that Δ_{47} derived temperature from soil carbonates were generally hotter than mean annual temperatures, but correlate well with warm summer month average temperatures(6). A modern soil carbonate from the Badan Jarain Desert in China run as part of this study also conforms to this relationship (Table S2-S3; Fig. S4).

We used data from the Yan An (Shaanxi Province) climate station (36.6°N, 109.5°E, 959 m) for comparison due to its relatively close proximity to Puxian and similar altitude. These data show that summer time (JJA) daily maximum temperatures in this region peak at over 30°C and average 28.8 ± 1.4°C (one standard deviation) for the years 2007-2010, whereas mean summertime daily temperatures are in the order of 23-25°C and average 23.3 ± 1.1°C. MJJAS are the months with a highest rainfall, as

expected in a monsoonal region, with July to October the most humid (Fig. S3). In contrast the coldest five months of the year generally have average daily temperature of ≤6°C and very little rainfall (Fig S5) Therefore given the strong seasonality in both temperature and rainfall it appears a robust assumption that the predominant, if not exclusive, period of growth of both soil carbonates and gastropods at Puxian is the warmest and wettest summer months.

In a recent study Zaarur et al., 2011 presented the first investigation of the relationship between Δ_{47} measurements from terrestrial gastropod shells and environmental temperatures(41). They studied 10 different taxa from 12 different locations, including tropical, desert, and temperate environments. Perhaps unsurprisingly they did not find a universal relationship between Δ_{47}-derived gastropod calcification temperatures and environmental temperature that held across all taxa and environments, and often calcification temperature were hotter than average environmental temperatures during the expected growing season. This was not attributed to a kinetic isotope effect, or "vital effect" on ^{13}C-^{18}O bond abundance in terrestrial gastropods, but the authors concluded that it was most likely a results of species and location specific differences in the timing of calcification and between the optimum growth temperatures of different taxa. However, when excluding data from their study from samples that are from arid environments (where winter is wettest season and the warmest months are dry) a correlation with environmental temperatures is observed (Fig S6). Therefore in environments most similar to monsoonal China (ie. Where the warmest months are also wet) it appears that gastropod calcification temperatures are correlated with environmental temperatures (Fig S6). However calcification temperatures are generally hotter than both mean annual temperatures and warm month average temperature, correlating most closely with average daily high temperatures (Fig S6). This is an indication that terrestrial gastropods must have a warm affinity for optimum growth, an observation that has been born out by culturing experiments on both shell forming and non-shell forming gastropod taxa (eg.(42, 43)).

Therefore despite uncertainties on the precise relationship between gastropod calcification temperatures and climatological data its clear that they have the potential to archive climate information and in particular data on temperature change over time when considering the same taxa and locality as this reduces the potential for species specific or inter-location effects. From our Δ_{47} measurements from modern *Cathaica* shells from Puxian we derive a temperature of 31.2 ± 1.5°C (2 s.e.) which correlate with daily summertime maximum temperatures (Fig S5-S7). Crucially we find that glacial specimens of *Cathaica* record a significantly colder temperature of 24.2 ± 1.9°C. It seems unlikely that this could reflect a lengthening of the growing season of *Cathaica* at the LGM as given its apparent affinity for warm conditions for optimum growth and if anything it might be expected to have a shorter summer growing season at the LGM.

As gastropod shells are likely to integrate climate information over a much shorter time period and than nodular soil carbonates we took the approach of measuring a large number of individual shells (>32). The necessity of large numbers of numbers of replicate measurements to gain significant constraints of temperature is illustrated by the relatively higher variability of gastropod derived Δ_{47} (Table S1-S3; Fig. S7). The high inter-individual variability seen in our gastropod Δ_{47} data may also go some way to explaining the scatter in the modern day calibration study. As least squared linear regression lines

through the modern gastropod calibration dataset have relatively large uncertainties in slope (Fig. S7) we did not attempt to develop a transfer function to relate calcification temperatures to environmental temperatures and instead chose to simply quote the data as "gastropod calcification temperatures" (Table 1), a change in which from LGM to present would clearly relate to a change in warm summer month temperatures.

Ultimately a crucial test of our assumptions on the systematics of interpreting temperatures from both soil carbonate and gastropod Δ_{47} measurements is whether they give mutually consistent results. The fact that they both give the same answer, within error, suggests that our approach is robust enough for our main objective which is distinguishing between lower magnitudes of cooling (2-3°C) °C and greater than 5°C of temperature change that allows us to critically evaluate model outputs and previous interpretations of proxy data.

B2. Isotope flux models of terrestrial gastropod body water

We used the land snail isotope flux model of Balakrishnan and Yapp, 2004 to constrain changes in precipitation $\delta^{18}O$ using our reconstructed values of gastropod body water $\delta^{18}O$(44). The water input is from surface water that the snail body comes in contact with. Thus, their main water source is surface water collected on the ground. As land snails are active during and following rain events, this surface water should be isotopically close to rainwater. The aragonite shells of snails are precipitated from body water assumed to be at an isotopic steady state(44). The main water loss is through the evaporation of body water into the atmosphere. Assuming that the direct loss of liquid water is negligible compared to the loss due to evaporation, the snail isotope model is equivalent to the Craig-Gordon model(45) commonly applied to evaporation from lakes and leaves. At a steady state, the isotopic composition of snail body water (R_{sbw}) is calculated as:

$$R_{sbw} = \alpha_{wv} (\alpha_k (1 - h_{surf}) R_{surf} + h_{surf} R_{vap})$$

where h_{surf} is the relative humidity of the snail habitat, α_k is the kinetic fractionation during evaporation (1.0285)(46), and α_{wv} is the temperature-dependent equilibrium fractionation between liquid water and vapor(47). R_{surf} and R_{vap} are the isotopic composition of surface water and local water vapor, respectively. For the high humidity surface habitat of snails, we assume that atmospheric vapor is in isotopic equilibrium with the surface water ($R_{vap} = R_{surf} / \alpha_{wv}$) so that snail body water can be approximated as:

$$R_{sbw} = (\alpha_{wv} \alpha_k (1 - h_{surf}) + h_{surf}) R_{surf}$$

Using the mean $\delta^{18}O$ of summer (JJA) precipitation, approx. -7.1‰, as $\delta^{18}O_{surf}$ for the sample site at present-day conditions yields a local relative humidity of 0.82 to explain the $\delta^{18}O_{sbw}$ values of modern snails. This is close to the nighttime humidity range of 0.85 to 0.95 considered optimal for snail farming(48).

The LGM-modern shift in $\delta^{18}O_{sbw}$ reflects three factors: (1) changes in α_{wv} caused by changes in temperature, (2) changes in the local relative humidity h_{surf} of the snail habitat, and/or (3) changes in $\delta^{18}O_{surf}$ related to mean summer precipitation. Temperature related changes in α_{wv} are usually small, only about 0.5‰ (Table S7). If the only change

in $\delta^{18}O_{surf}$ at the LGM was the 1.2‰ enrichment due to the increase in global ice volume, to explain the observed $\delta^{18}O_{sbw}$ difference would require a shift to substantially higher h_{surf} (Table S7). However, a higher local relative humidity at the LGM is unlikely given the generally drier climate compared to present-day conditions.

For the more plausible assumption that the local relative humidity of the snail habitat was the same (or slightly drier) at the LGM, the observed $\delta^{18}O_{sbw}$ difference requires large changes in the isotopic composition of surface water, and hence precipitation. For constant h_{surf}, the resulting $\delta^{18}O_{surf}$ was approximately 5.2‰ lighter at the LGM (also including ice-volume correction), which we assume is the most likely outcome. If we assume a reduction in relative humidity by 5%, then we calculate an LGM $\delta^{18}O_{surf}$ that was 7.1‰ lighter at the LGM (Table S7) which is a significant mismatch to soil carbonate data and model results and so is probably an indication that humidity in the snail microenvironment was buffered and stable from LGM to present. Using $\delta^{18}O_{rain}$ data from nearby GNIP (Global Network of Isotopes in Precipitation) sites yields a range of possible $\delta^{18}O$ values for precipitation during the LGM, however, the LGM-modern $\delta^{18}O$ difference is constant irrespective of the site (Table S8). Thus, the change in body water $\delta^{18}O$ of snails indicates a substantial shift in the $\delta^{18}O$ of mean summer precipitation towards LGM values that were depleted by at least ~5.2‰, relative to present according to this model of body waters (Fig. S8).

B3. Analysis of PMIP2 model output

We have analyzed the northern-hemisphere summer (JJA) stationary wave response in PMIP2 model simulations of the LGM in order to give context to our simulations with the LMD models. The JJA stationary wave response in each model is demonstrated by differencing LGM simulations and the same model under present-day (PD) conditions. Fig. S3 displays LGM-PD of the 500-hPa wind and surface temperature anomalies for JJA. Circulating wind vectors indicate the enhancement of stationary waves in the LGM versus PD. Regions with enhanced cyclonic (CCW) winds roughly coincide with regions of enhanced cooling, demonstrating the importance of stationary waves for regional climate sensitivity in these models.

The HadCen (oav) and FGOALS models stand out as having enhanced high-latitude cooling relative to the others. The HadCen model, however, shows more than double the cooling at Puxian (-5.9ºC) as compared to FGOALS (-2.65ºC). In the 500-hPa wind anomalies, the HadCen (oav) has a much more pronounced and southward-shifted cyclonic (CCW) circulation north of Puxian. This dynamic feature advects cool air from the north towards Puxian. In addition, the IPSL simulation has enhanced cooling at Puxian (-5.74ºC), and also shows evidence for an enhanced cyclonic circulation north of Puxian (Figure 2). This feature north of Puxian is present in the simulation in our study (see Figure 1 in main text), and is responsible for the enhanced northwesterlies at Puxian.

B4. Comparisons of LMDZ simulations with clumped isotope data

The zoomed model simulations predict a mean annual temperature change of -6.4°C from the present to the LGM, and a mean summer temperature change of -6.3°C. This is consistent with the reconstructed temperature change of -7+/-2°C from terrestrial gastropods and -5.5 ± 2.0°C from soil carbonates. The zoomed simulations predict a

decrease in mean annual precipitation $\delta^{18}O$ of -3.3‰ (with ice-volume correction), which is comparable to the reconstructed value of -2‰ from soil carbonates and -5.2‰ from snails.

The standard simulations with the LMDZ model predicts changes in mean annual temperature and precipitation $\delta^{18}O$ of -8.2°C and -2‰ after ice-volume correction) respectively. As discussed in the main text, within error temperature estimates from gastropods and soil carbonate are consistent with both LMDZ simulations, and suggest a greater magnitude of cooling than most PMIP2 models suggest. Both model simulations and proxy archives support a shift towards lighter isotopic composition of precipitation at the LGM, but differ in the precise value. Therefore we can validate this fundamental result in our model, and go on to interrogate the causes of isotope shifts in our model output, but cannot constrain which of the two LMDZ simulations is closest to the true value.

B5. Causes of temperature changes in LMDZ simulations

The temperature change at the LGM compared to present is amplified with altitude and latitude (Fig. S5). The amplification with altitude has already been documented in syntheses of tropical terrestrial records such as that of Farrera et al., 1999(49). It can be explained by the weakening of the atmospheric lapse rate, which follows a moist adiabat in the tropics[42]. Iso-contours of temperature changes are closed to horizontal in the tropics, and their intersection with the topography explain the amplification of temperature changes at higher elevation (Fig. S11). The amplification with latitude has also been documented by data syntheses such as that of Shakun and Carlson, 2010(50). LMDZ simulates a cooling of of -2 to -3°C in the Western Pacific, in agreement with the data synthesized by Shakun and Carlson, 2010 (50). At the longitude of Puxian, as for the rest of the globe, the LGM cooling increases with latitude up to -12°C at 60°N.

To understand this amplification with altitude, we performed a radiative kernel decomposition of the climate sensitivity(51). This method allows us to quantify the radiative feedbacks of surface temperature changes on top-of-the-atmosphere radiation associated with different processes: water vapor feedback, lapse rate feedback, cloud feedbacks and surface albedo feedbacks. This method had already been used successfully to analyze the climate sensitivity for both future(51) and LGM(52) changes. Results show that the surface albedo feedback increases with latitude and exhibits a secondary peak on the Tibetan plateau (Fig. S11). Therefore, the albedo feedback is likely the major contribution to the amplification of temperature changes with latitude and altitude. It is associated with enhanced snow cover at LGM. Note that this decomposition method does not take into account the effects of large-scale circulation.

In addition, the changes in large-scale circulation amplify the LGM cooling. To support this we compare PMIP2 models and LMDZ and relate their LGM-PD cooling at Puxian to the magnitude of northerly wind to the Northwest of Puxian. Figure 2 in the main text shows a clear correlation between 500-hPa, JJA northerly winds averaged over 40N-50N latitude and 80E-110E longitude and simulated cooling at Puxian, LGM-PD. Enhanced northerly flow results in enhanced advective cooling from the region north of Puxian. From inspection of Fig. S3, we conclude these northerly winds are associated with continental-scale stationary waves, thereby directly linking the regional climate

sensitivity of East Asia to large-scale dynamics. A simulation without ice-sheets (ie. with present-day topography and land ice fraction) exhibited suppressed stationary waves at the LGM. This simulation exhibited ~30% less cooling than the standard LGM LMDZ simulation, an indication that stationary waves enhanced by continental ice-sheets are a significant factor in cooling at the site (Fig. 2; Fig. S9)

Somewhat counter-intuitively, LGM with PD land albedo gives the strongest northwesterly winds at Puxian of any model, and interactive land albedo reduces the northwesterlies (and associated Puxian cooling) in the LMDZ model. The LGM-PD anomalies for a set of sensitivity runs (Fig. S9) help to clarify. In particular, the "LGM w/PD albedo" (top right panel) has very clean-looking mid-latitude stationary waves with obvious correlations in surface temperature anomalies, especially over East Asia. In comparison, stationary waves in the standard LGM case with interactive land albedo (top left panel) are clearly apparent but not as organized over mid-latitude Asia, and in particular the cooled region over East Asia is more compact in the PD-albedo case. Removing the ice sheets (bottom panel) very substantially reduced the amplitude of the stationary wave response. Taken together, our analyses suggests the LGM cooling at Puxian is dominated by stationary waves, and interactive land feedback can either enhance or reduce this cooling.

B6. Causes of water $\delta^{18}O$ changes in high-resolution simulation

Proposed major controls on precipitation $\delta^{18}O$ ($^{18}O_p$) in this monsoon region (e.g. (35, 53)) include either local effects (e.g.(54)), or through isotopic depletion along air mass trajectories (e.g.(35)). Here we focus on understanding the LGM-PD difference of JJA mean precipitation, which is the time recorded by proxies. The high-resolution simulations indicate decreased LGM water $\delta^{18}O$ may originate due to the (1) decrease in local temperature associated with the altitudal and latitudal amplification of LGM cooling, (2) decrease in last condensation temperature associated with the weakening lapse-rate in the tropical troposphere, (3) circulation changes that bring more dry and depleted air from the North-West, and (4) $\delta^{18}O_p$ recording vapor $\delta^{18}O$ ($\delta^{18}O_v$) changes at the condensation level where $\delta^{18}O_v$ changes are amplified due to (1) and (2).

The change in mean annual $\delta^{18}O_p$ can be decomposed into changes of $\delta^{18}Op$ in the different seasons and changes in the precipitation seasonality. Changes in the seasonality of precipitation on the Loess Plateau explain only 11% of the simulated annual-mean $\delta^{18}O_p$ change. Most of the change in mean annual $\delta^{18}O_p$ is explained by changes in $\delta^{18}O_p$ in June-July-August (JJA, 23%) and in September-October-November (SON, 67%). This is because half of the precipitation in Puxian in the model falls in JJA, and the other half in SON, and changes in $\delta^{18}O_p$ are largest in SON.

The simulated -3.3‰ change in JJA-mean $\delta^{18}O_p$ in the zoomed simulation (after correction for sea-water change) can be decomposed into 2 components: a component related to the change in the ($\delta^{18}O_v$), which is controlled by large-scale processes, and a change in the difference between $\delta^{18}O_p$ and $\delta^{18}O_v$. The change in $\delta^{18}O_v$ explains 87% (-2.9‰) of the $\delta^{18}O_p$ change. In addition, spatial patterns of $\delta^{18}O_p$ changes are similar to those in $\delta^{18}O_v$ (Fig S12). Therefore, most of the following paragraphs will focus on understanding the change in $\delta^{18}O_v$ in JJASON.

In LMDZ at LGM, precipitation increases over Northern India and over Burma (Fig. S12). This leads to a depletion of $\delta^{18}O_p$ in these regions, but the effect on $\delta^{18}O_v$ is very limited (Fig S12). The $\delta^{18}O_p$ depletion is not due to the depletion of the vapor, but to the decrease of rain reevaporation in a moister atmosphere leading to more depleted precipitation relatively to the vapor(29, 55). In LMDZ, the effect of precipitation on $\delta^{18}O_p$ is thus restricted to convective regions, and is not exported up to higher latitude sites such as Puxian. This suggests that precipitation changes are not responsible for the observed δ^{18}Op change. However, LMDZ has been suspected to overestimate the local controls of convection on $\delta^{18}O_p$ and underestimate its remote effects through δ^{18}Ov(39). Therefore, we cannot rule out a small contribution of the precipitation increase over India to the $\delta^{18}O_p$ decrease at Puxian, as suggested by Pausata et al., 2011(35).

The pattern of $\delta^{18}O_v$ change exhibits similarities with that of temperature changes (Fig. S12). Cooling and depletion are both largest over the Tibetan plateau and at high latitude. This suggests that the temperature change is a factor responsible for the $\delta^{18}O_v$ change. However, the most striking similarity of patterns in between $\delta^{18}O_v$ changes and relative changes in specific humidity (dq/q, where q is the specific humidity) (Fig. S12). The spatial correlations in the Puxian region between $\delta^{18}O_v$ changes and dq/q are 0.79, while the spatial correlation between $\delta^{18}O_v$ changes and temperature changes are 0.35 in JJA. The good relationship between δ^{18}Ov changes and $\Delta q/q$ is predicted by Rayleigh distillation:

$$R_v = R_v0*(q/q0)**(alpha-1) \quad \text{(Eq 1)}$$

where R_v and q are the isotopic ratio and specific humidity of the distilled air vapor, R_v0 and q0 are the isotopic ratio and specific humidity of the initial vapor, and alpha is the fractionation coefficient. For small changes in q and R_v, we get:

$$\Delta\delta^{18}O_v \sim \Delta R_v/R_v*1000 = (alpha-1)*1000*\Delta q/q \quad \text{(Eq 2)}$$

The slope of the simulated spatial relationship $\Delta q/q$ is about 8‰ in JJA This is thus consistent with the order of magnitudes of the predicted slope of (alpha-1)*1000, which is 9.5+/-3 permil for Puxian PD and LGM temperatures.

Simulated $\delta^{18}O_v$ changes correlate much better with dq/q than with temperature changes because both specific humidity and $\delta^{18}O_v$ depend on the temperature during the last condensation event(56, 57), which can be different from the local temperature. For example, the amplification of temperature changes with altitude is restricted to low latitude (equatorward of about 35°C, Fig. S11). In contrast, the amplification of dq/q and $\delta^{18}O_v$ changes with altitude holds at all latitudes including that of Puxian. This is because the dry and depleted anomalies associated with colder temperature temperatures in the tropical-subtropical upper-troposphere, where condensation occurs, are propagated poleward by the mean flow.

Also, the circulation changes discussed in section B5 likely contribute to the drying and to the depletion of the water vapor at Puxian at LGM, due to the stronger northwesterly component of the winds at LGM (Figure 3 of main text).

Finally, we mentioned that the decrease in $\delta^{18}O_v$ explains only 87% of the

decrease in $\delta^{18}O_p$. The remaining 13% are due to the altitude amplification of $\delta^{18}Ov$ changes (Fig. S13). Most of the condensation over Puxian occurs between about 5 km and 10 km above ground level. Therefore, the precipitation at Puxian records a LGM-recent anomaly of the vapor at about 6 km (Fig. S13). This leads to additional 0.4‰ depletion in $\delta^{18}O_p$ compared to $\delta^{18}O_v$.

Supplementary references

1. Kukla G (1987) Loess stratigraphy in central China *Quatern. Sci. Rev.* 6(3-4):191-207.
2. Kukla G & An Z (1989) Loess stratigraphy in central China *Palaeogr. Palaeoclimatol. Palaeoecol.* 72:203-225.
3. Ding ZL*, et al.* (2002) Stacked 2.6-Ma grain size record from the Chinese loess based on five sections and correlation with the deep-sea $\delta^{18}O$ record. *Paleoceanography* 17(3):10.1029/2001PA000725.
4. Sheng X, Chen J, Cai Y, Chen Y, & Ji J (2005) Aragonite-calcite transformation in fossil snail shells of loess sequences in Loess Plateau, Central China. *Chinese Science Bulletin* 50:891-895.
5. Rao Z, Zhu Z, Chen F, & Zhang J (2006) Does delta-^{13}Ccarb of the Chinese loess indicate past C_3/C_4 abundance? A review of research on stable carbon isotopes of the Chinese loess. *Quatern. Sci. Rev.* 25:2251-2257.
6. Passey BH, Levin NE, Cerling TE, Brown FH, & Eiler JM (2010) High-temperature environments of human evolution in East Africa based on bond ordering in paleosol carbonates. *Proc. Natl. Acad. Sci. USA* 107(25):11245-11249.
7. Affek H & Eiler JM (2006) Abundance of mass 47 CO2 in urban air, car exhaust, and human breath *Geochim. Cosmochim. Acta* 70(1):1-12.
8. Huntington KW*, et al.* (2009) Methods and limitations of 'clumped' CO_2 isotope (Delta47) analysis by gas-source isotope ratio mass spectrometry. *J. Mass Spectrom.* 44(9):1318-1329.
9. Eiler JM & Schauble E (2004) $^{18}O^{13}C^{16}O$ in Earth's atmosphere. *Geochim. Cosmochim. Acta* 68(23):4767-4777.
10. Ghosh P*, et al.* (2006) $^{13}C–^{18}O$ bonds in carbonate minerals: a new kind of paleothermometer. *Geochim. Cosmochim. Acta* 70(6):1439-1456.
11. Guo W, Mosenfelder JL, Goddard III WA, & Eiler JM (2009) Isotopic fractionations associated with phosphoric acid digestion of carbonate minerals: insights from first-principles theoretical modeling and clumped isotope measurements. *Geochim. Cosmochim. Acta* 73(24):7203-7225.
12. Dennis KJ & Schrag DP (2010) Clumped isotope thermometry of carbonatites as an indicator of diagenetic alteration. *Geochim. Cosmochim. Acta* 74(14):4110-4122.
13. Tripati AK*, et al.* (2010) $^{13}C–^{18}O$ isotope signatures and 'clumped isotope' thermometry in foraminifera and coccoliths *Geochim. Cosmochim. Acta* 74(20):5697-5717.

14. Eagle RA, *et al.* (2010) Body temperatures of modern and extinct vertebrates from ^{13}C-^{18}O bond abundances in bioapatite. *Proc. Natl. Acad. Sci. USA* 107(23):10377-10382.
15. Thiagarajan N, Adkins J, & Eiler J (2011) Carbonate clumped isotope thermometry of deep-sea corals and implications for vital effects. *Geochim. Cosmochim. Acta* 75:4416-4425.
16. Dennis KJ, Affek HP, Passey BH, Schrag DP, & Eiler JM (2011) Defining an absolute reference frame for 'clumped' isotope studies of CO_2. *Geochim. Cosmochim. Acta* 75:7117-7131.
17. Kim S-T, Mucci A, & Taylor B (2007) Phosphoric acid fractionation factors for calcite and aragonite between 25 and 75 deg C. *Chem. Geol.* 246:135-146.
18. Swart PK, Burns SJ, & Leder JJ (1991) Fractionation of the stable isotopes of oxygen and carbon in carbon-dioxide during the reaction of calcite with phosphoric-acid as a function of temperature and technique. *Chem. Geol.* 86(2):89-96.
19. Kim S-T & O'Neil JR (1997) Equilibrium and nonequilibrium oxygen isotope effects in synthetic carbonates. *Geochim. Cosmochim. Acta* 61(16):3461-3475.
20. Braconnot P, *et al.* (2007) Results of PMIP2 coupled simulations of the Mid-Holocene and Last Glacial Maximum - Part 1: Experiments and large-scale features. *Clim. Past* 3:261-277.
21. Hourdin F, *et al.* (2006) The LMDZ4 general circulation model: Climate performance and sensitivity to parametrized physics with emphasis on tropical convection. *Clim. Dyn.* 27:787-813.
22. Marti O, *et al.* (2005) The New IPSL Climate System Model. *Tech. Rep., IPSLCM4, IPSL*.
23. Meehl GA, *et al.* (2007) The WCRP CMIP3 multimodel dataset:. *Bull. Amer. Met. Soc.* 88:1383-1394.
24. Van Leer B (1977) Towards the ultimate conservative difference scheme. IV. A new approach to numerical convection. *J. Comput. Phys.* 23:276-299.
25. Hourdin F & Armengaud A (1999) The use of finite volume methods for atmospheric advection of trace species. Part I: Test of various formulations in a general circulation model. *Mon. Wea. Rev.* 127:822-837.
26. Emanuel KA (1991) A scheme for representing cumulus convection in large-scale models. *J. Atmos. Sci.* 48:2313-2329.
27. Emanuel KA & Zivkovic-Rothman M (1999) Development and evaluation of a convection scheme for use in climate models. *J. Atmos. Sci.* 56:1766-1782.
28. Bony S & Emanuel KA (2001) A parameterization of the cloudiness associated with cumulus convection; Evaluation using TOGA COARE data. *J. Atmos. Sci.* 58(3158-3183).
29. Risi C, Bony S, Vimeux F, & Jouzel J (2010) Water stable isotopes in the LMDZ4 General Circulation Model: model evaluation for present day and past climates and applications to climatic interpretation of tropical isotopic records. *J. Geophys. Res.* 115:D12118, doi:12110.11029/12009JD013255.
30. Gates WL (1992) AMIP: The Atmospheric Model Intercomparison Project. *Bull. Am. Meteorol. Soc.* 73:1962-1970.
31. Steen-Larsen HC, *et al.* (2011) Understanding the climatic signal in the water

stable isotope records from the NEEM shallow firn/ice cores in northwest Greenland. *J. Geophys. Res.* 116:D06108; doi:06110.01029/02010JD014311
32. Gao J*, et al.* (2011) Precipitation Water Stable Isotopes in the South Tibetan Plateau: Observations and Modeling. *J. Climate* 24:3161-3178.
33. Risi C (2012) Process-evaluation of tropospheric humidity simulated by general circulation models using water vapor isotopologues. Part 1: comparison between models and observations. *J. Geophys. Res.* 117: DOI: 10.1029/2011JD016621
34. Lee JE, Fung I, DePaolo DJ, & Otto-Bliesner B (2008) Water isotopes during the Last Glacial Maximum: New general circulation model calculations. *J. Geophys. Res.* 113:D19109, doi:19110.11029/12008JD009859.
35. Pausata FR, Battisti DS, Nisancioglu KH, & Bitz CM (2011) Chinese stalagmite $\delta^{18}O$ controlled by changes in the Indian monsoon during a simulated Heinrich event *Nat. Geosci.* 4:474-480.
36. Berger AL (1978) Long-term variations of caloric insolation resulting from the earth's orbital elements. *Quatern. Res.* 9:139-167.
37. Peltier WR (1994) Ice age paleotopography. *Science* 265:195-201.
38. Labeyrie LD, Duplessy JC, & Blanc PL (1987) Variations in mode of formation and temperature of oceanic deep waters over the past 125,000 years. *Nature* 327:477-482.
39. Vimeux F, Tremoy G, Risi C, & Gallaire R (2011) A strong control of the South American SeeSaw on the intra-seasonal variability of the isotopic composition of precipitation in the Bolivian Andes. *Earth Planet. Sci. Lett.* 307:47-58.
40. Breecker D, Sharp ZD, & McFadden L (2009) Seasonal bias in the formation and stable isotope composition of pedogenic carbonate in modern soils from central New Mexico. . *GSA Bulletin* 121:630-640.
41. Zaarur S, Olack G, & Affek HP (2011) Paleo-environmental implication of clumped isotopes in land snail shells *Geochim. Cosmochim. Acta* 75(22):6859-6869.
42. Aufderheide J*, et al.* (2006) Effects of husbandry parameters on the life-history traits of the apple snail, Marisa cornuarietis: effects of temperature, photoperiod, and population density. *Invertebrate Biology* 125(1):9-20.
43. Rising TL & Armitage KB (1969) Acclimation to temperature by the terrestrial gastropods, *Limax maximus* and *Philomycus carolinianus*: oxygen consumption and temperaature preference. *Comp. Biochem. Physiol.* 30:1091-1114.
44. Balakrishnan M & Yapp CJ (2004) Flux balance models for the oxygen and carbon isotope compositions of land snail shells. *Geochim. Cosmochim. Acta* 68(9):2007-2024.
45. Craig H & Gordon LI (1965) Deuterium and oxygen 18 variations in the ocean and marine atmosphere. *proc. Stable Isotopes in Oceanographic Studies and Paleotemperatures*, (V. Lishi e F., Pisa., Spoleto, Italy), pp 9-130.
46. Merlivat L (1978) Molecular diffusivities of $H_2{}^{16}O$, $HD^{16}O$, and $H_2{}^{18}O$ in gases. . *J. Chem. Phys.* 69:2864–2871.
47. Majoube M (1971) Fractionnement en oxygen-18 et en deuterium entre l'eau et sa vapeur. *J. Chem. Phys.* 68:1423-1436.
48. Thompson R & Cheny S (1996) *Raising snails* (National Agriculture Library Special reference briefs. , NAL SRB 96-05).

49. Farrera I*, et al.* (1999) Tropical climates at the Last Glacial Maximum: a new synthesis of terrestrial palaeoclimate data. I. Vegetation, lake-levels and geochemistry. *Clim. Dyn.* 15(823-856).
50. Shakun JD & Carlson AE (2010) A global perspective on Last Glacial Maximum to Holocene climate change *Quatern. Sci. Rev.* 29:1801-1816.
51. Soden BJ*, et al.* (2008) Quantifying Climate Feedbacks Using Radiative Kernels. *J. Climate* 21:3504-3520.
52. Yoshimori M, Yokohata T, & Abe-Ouchi A (2009) A Comparison of Climate Feedback Strength between CO2 Doubling and LGM Experiments. *J. Climate* 22:3374-3395.
53. Wang Y*, et al.* (2008) Millennial- and orbital-scale changes in the East Asian monsoon over the past 224,000 years. *Nature* 451:1090-1093.
54. Dansgaard W (1964) Stable isotopes in precipitation. *Tellus* 16:436-468.
55. Risi C, Bony S, Vimeux F, Chong M, & Descroix L (2010) Evolution of the water stable isotopic composition of the rain sampled along Sahelian squall lines. *Q. J. R. Meteorol. Soc.* 136:227-242.
56. Galewsky JA, Sobel A, & Held I (2005) Diagnosis of subtropical humidity dynamics using tracers of last saturation. *J. Atmos. Sci.* 62:3353-3367.
57. Galewsky J & Hurley JV (2010) An advection condensation model for subtropical water vapor isotopic ratios. *J. Geophys. Res.* 115(D16116):doi:10.1029/2009JD013651.
58. Thompson LG*, et al.* (1997) Tropical Climate Instability: The Last Glacial Cycle from a Qinghai-Tibetan Ice Core. *Science* 276:1821-1825.
59. Thompson LG*, et al.* (1989) Holocene-Late Pleistocene Climatic Ice Core Record from Qinghai-Tibetan Plataeu. *Science* 246:474-477.
60. Wang YJ*, et al.* (2001) A high-resolution absolute dated Late Pleistocene Monsoon Record from Hulu Cave, China. *Science* 294:2345-2348.
61. Dykoski CA*, et al.* (2005) A high-resolution, absolute-dated Holocene and deglacial Asian monsoon record from Dongge Cave, China. *Earth Planet. Sci. Lett.* 233:71-86.

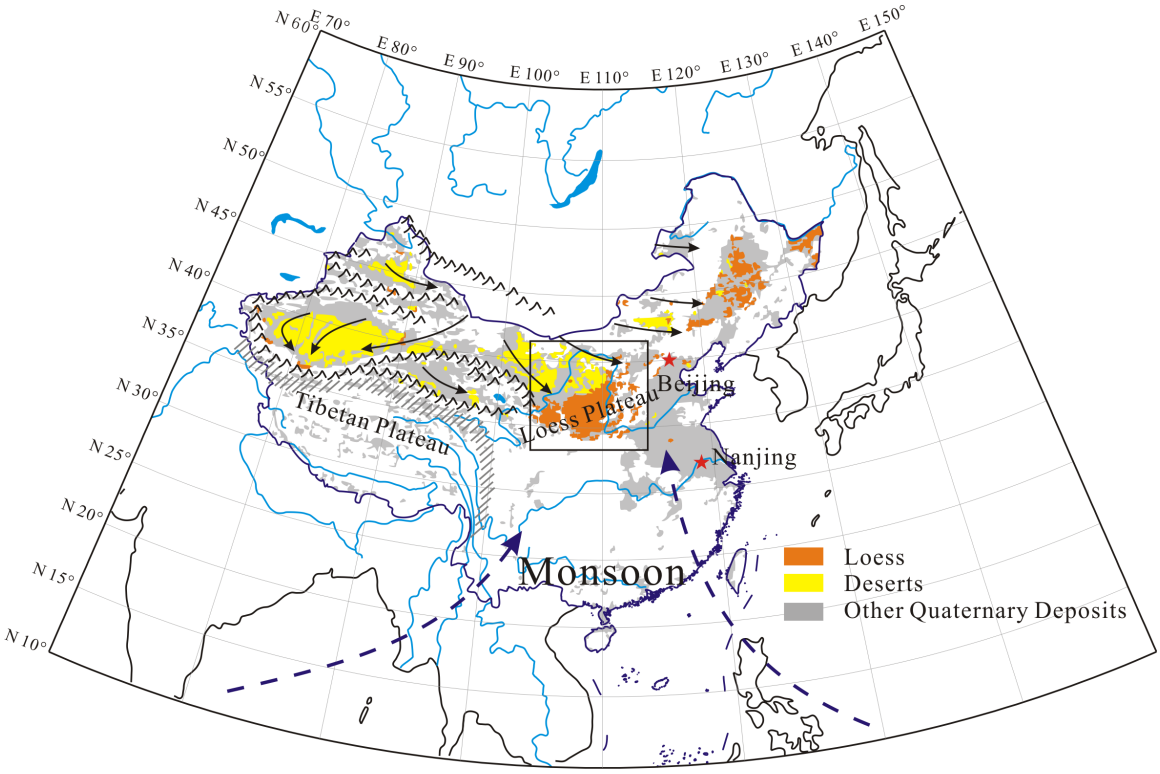

Fig. S1: Map showing the central Chinese Loess Plateau.

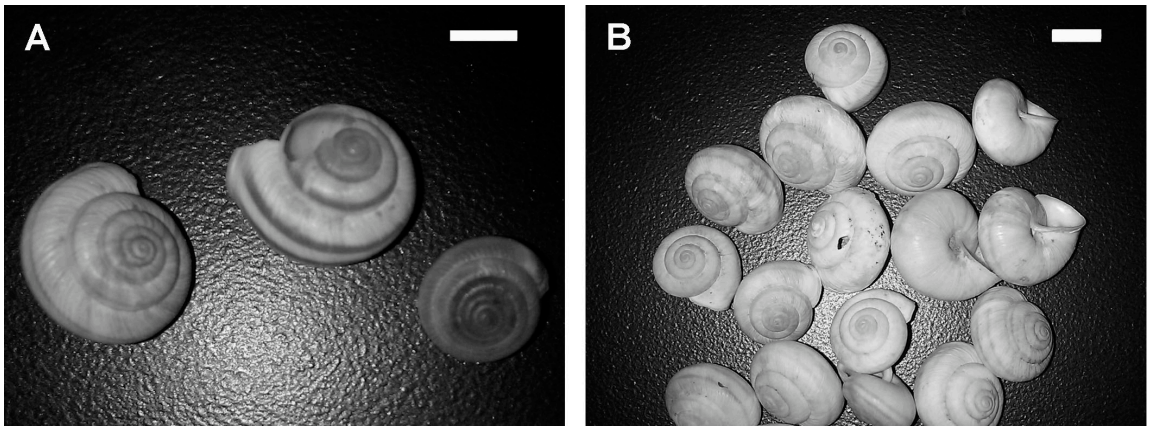

Fig. S2: Pictures of gastropod specimens. Scale bars represent 1 cm.

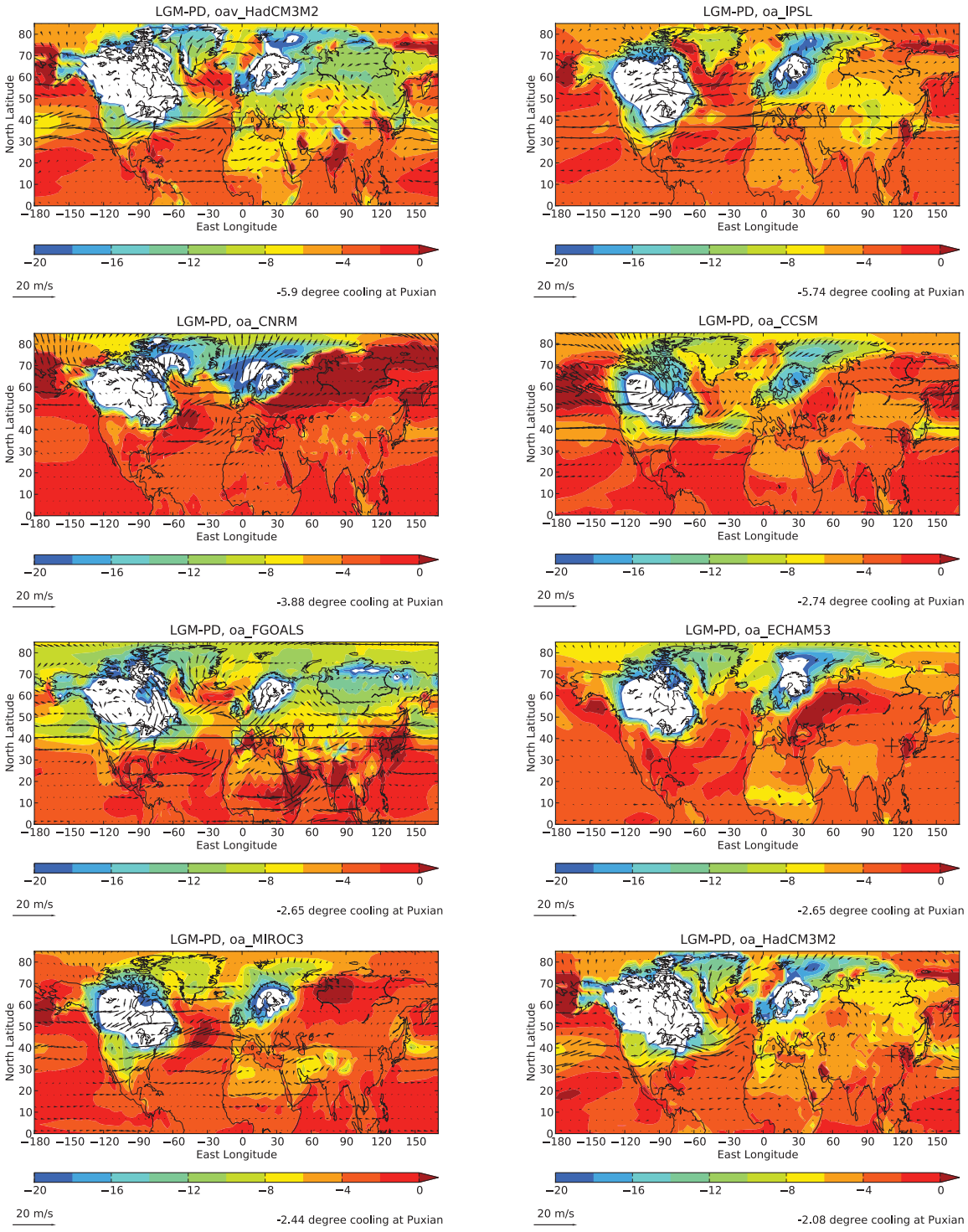

Fig. S3: Northern Hemisphere JJA surface temperature (colors) and 500-hPa wind anomalies for the Last Glacial Maximum-Present Day simulations (LGM-PD) for PMIP2 models, as labeled. White regions experience cooling in excess of 20ºC. The cooling at Puxian (marked with a cross) is indicated in the lower right of each panel.

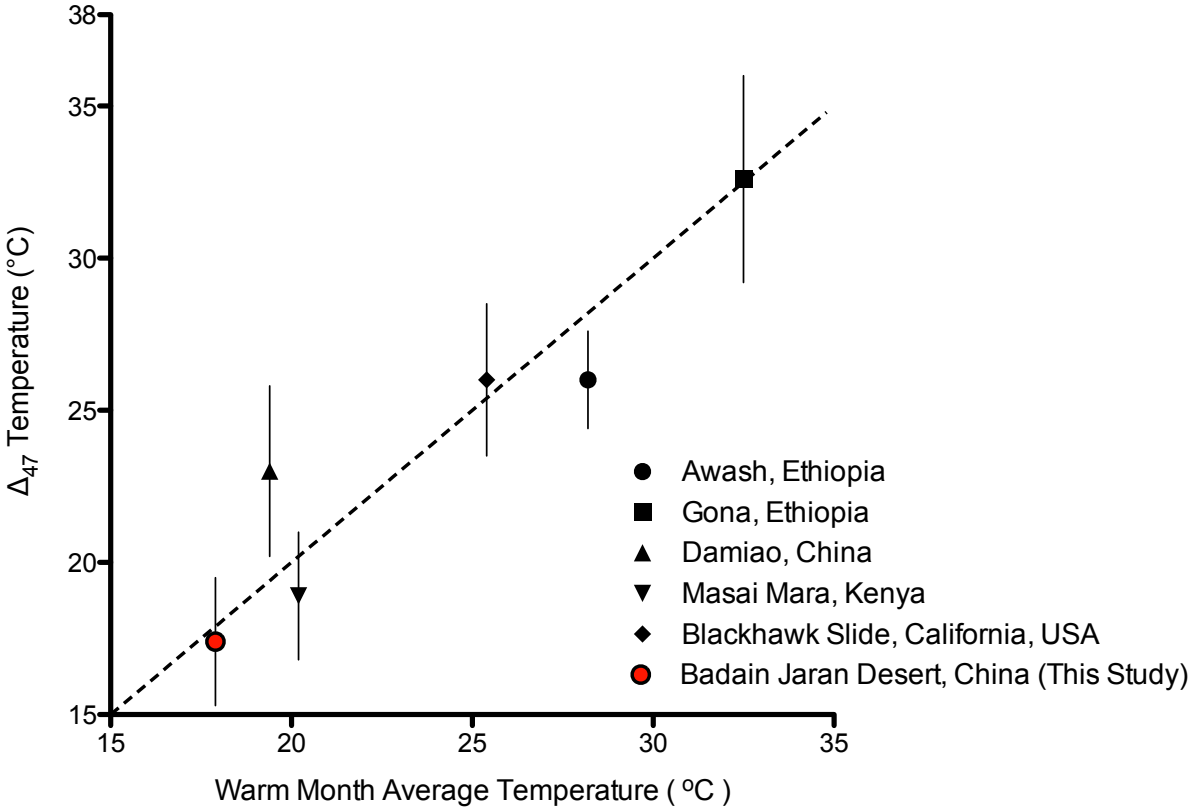

Fig. S4: Calibration of the clumped isotope paleothermometer in soil carbonates. Data from Passey et al., 2010 *(5)* are given in black, our data is shown as an open circle.

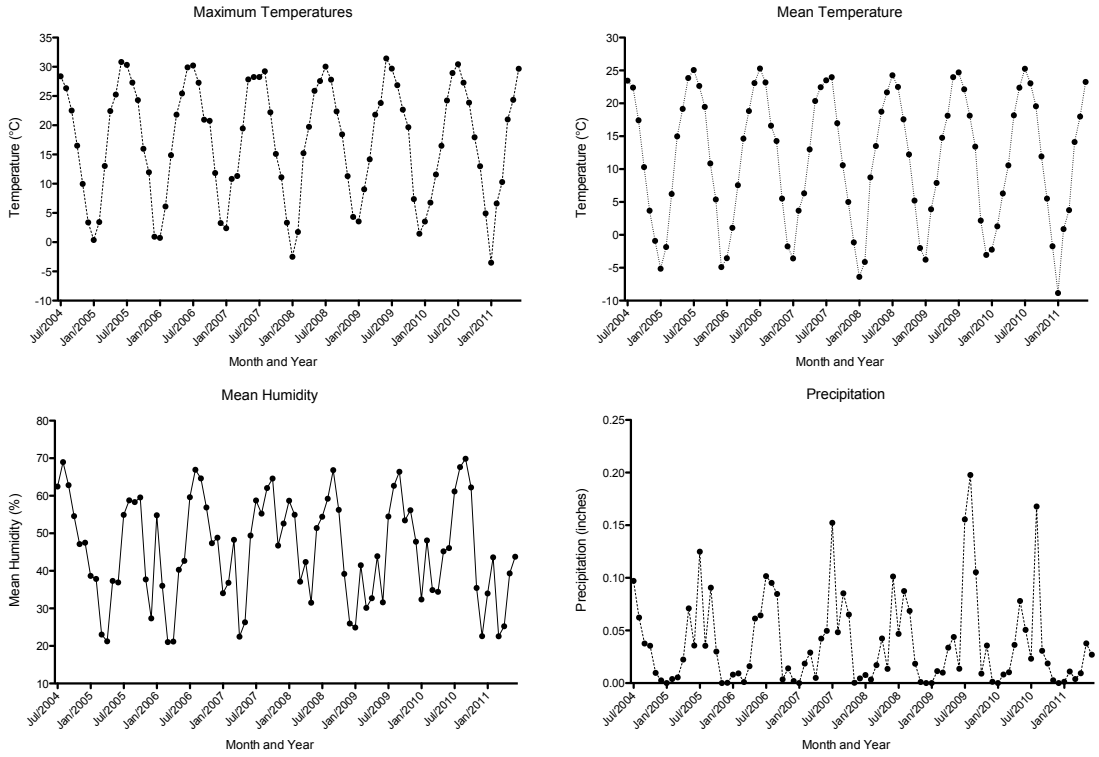

Fig. S5: Climatological data from station at Yan An, Shaanxi province.

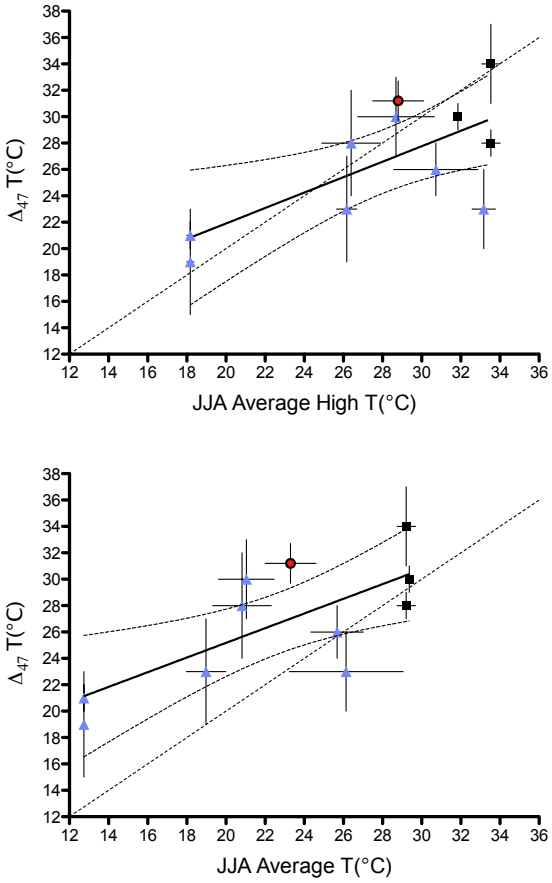

Fig. S6. Published terrestrial gastropod data *(40)* for sites with a warm rainy season and our data on modern land snails from Puxian. Δ_{47} derived temperatures are compared to summertime (June, July, August) average temperatures, and average daily high temperature. The slope of least-squares linear regression line (solid black line, dotted curved-lines are 95% confidence intervals) in both plots is clearly non-zero, indicating that terrestrial gastropod calcification temperatures are correlated with environmental temperatures. Data from tropical climates with weak seasonality in temperature, but with the summer months also having significant rainfall are plotted as black squares. Data from climates with strong seasonality in temperature, and with wet summers is plotted as purple triangles. Our data from Puxian is plotted as an open circle. Crucially we excluded data from arid/desert environments in California and Israel *(40)* that are characterized by arid summers; these sites are climatically the least similar to the climate of our study site and snails there may experience dessication and are therefore unlikely to calcify in the summer. For the top panel the slope of the regression = 0.585 ± 0.200, intercept = 10.200 ± 5.734, and the slope is significantly nonzero ($p = 0.0170$). For the bottom panel; slope = 0.556 ± 0.177, intercept = 14.050 ± 4.143, again the slope is significantly nonzero ($p = 0.0119$). Straight dotted lines show a 1:1 relationship.

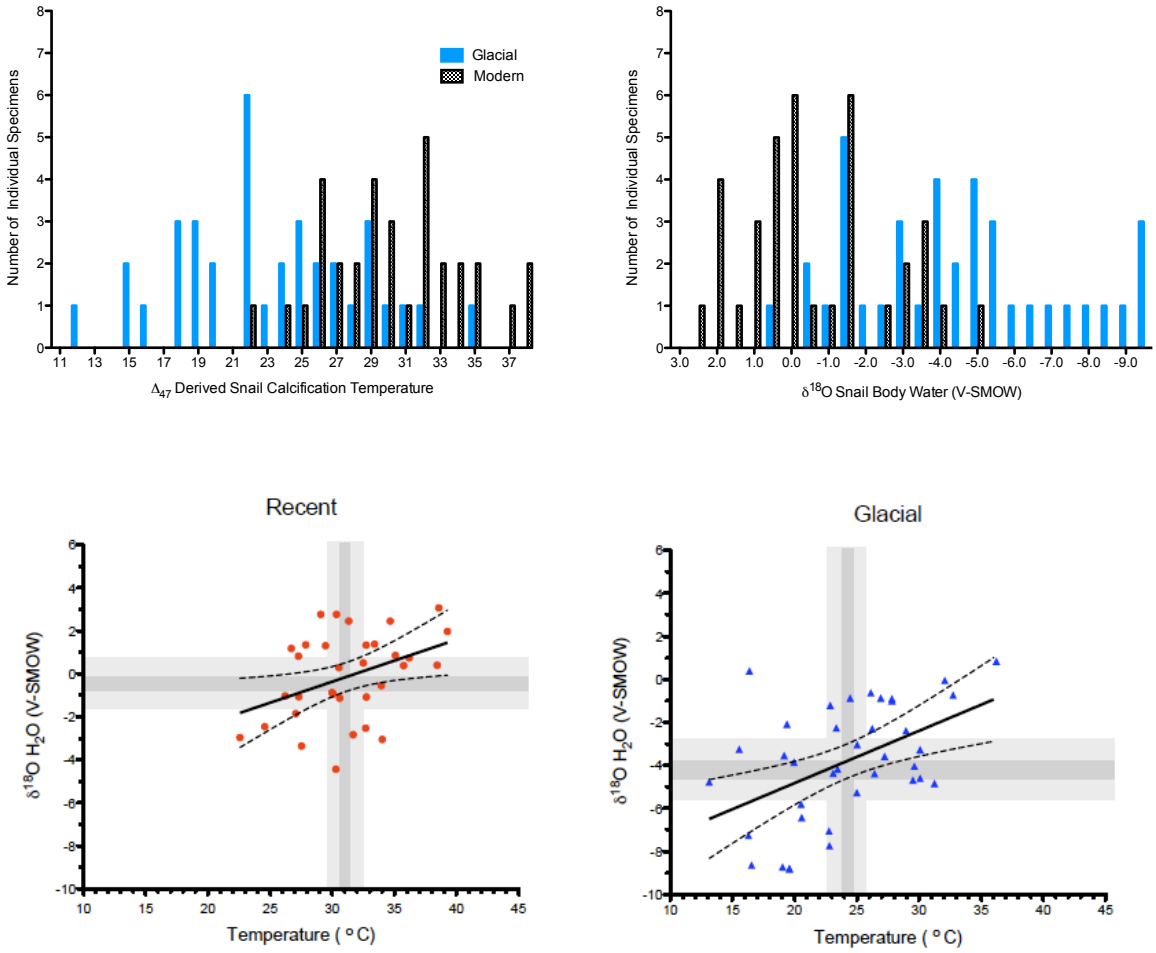

Fig. S7: Top panels: Histograms of gastropod derived temperature and water isotope data. The temperature data is indistinguishable from a normal distribution (Shapiro-Wilk test p value for modern = 0.92, glacial = 0.962, where the null hypothesis is that the data follows a normal distribution). Bottom panels: Scatter plots of the same data. Filled line is a linear regression through the data, dotted lines are 95% confidence intervals. The slope of the line through recent data is 0.20, the slope of the glacial is 0.24. Both slopes fall within the 95% confidence intervals of each other, as indicated by the dotted lines. Darker grey shaded areas indicate one standard error (s.e.) in temperature and gastropod body water $\delta^{18}O$, the lighter grey area is 2 s.e.

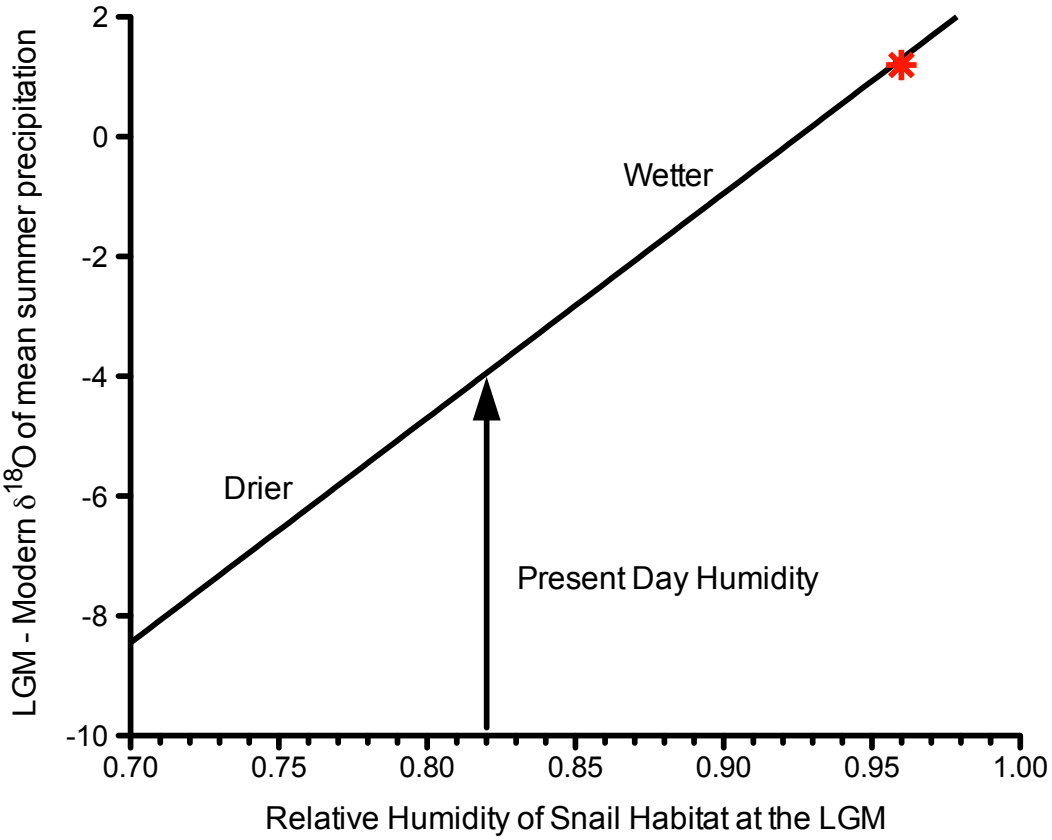

Fig. S8: Relationship between the calculated change in local precipitation $\delta^{18}O$ and relative humidity of snail habitats based on the isotope flux model of Balakrishnan and Yapp, 2004 *(43)*. The star indicates the humidity required to explain snail body water if the only change in precipitation was the 1.2‰ enrichment due to the larger global ice volume. As this would involve an increase in humidity at the Last Glacial Maximum, we consider this scenario to be unlikely. Therefore our data support a shift towards lighter isotopic composition of precipitation at Puxian at the Last Glacial Maximum.

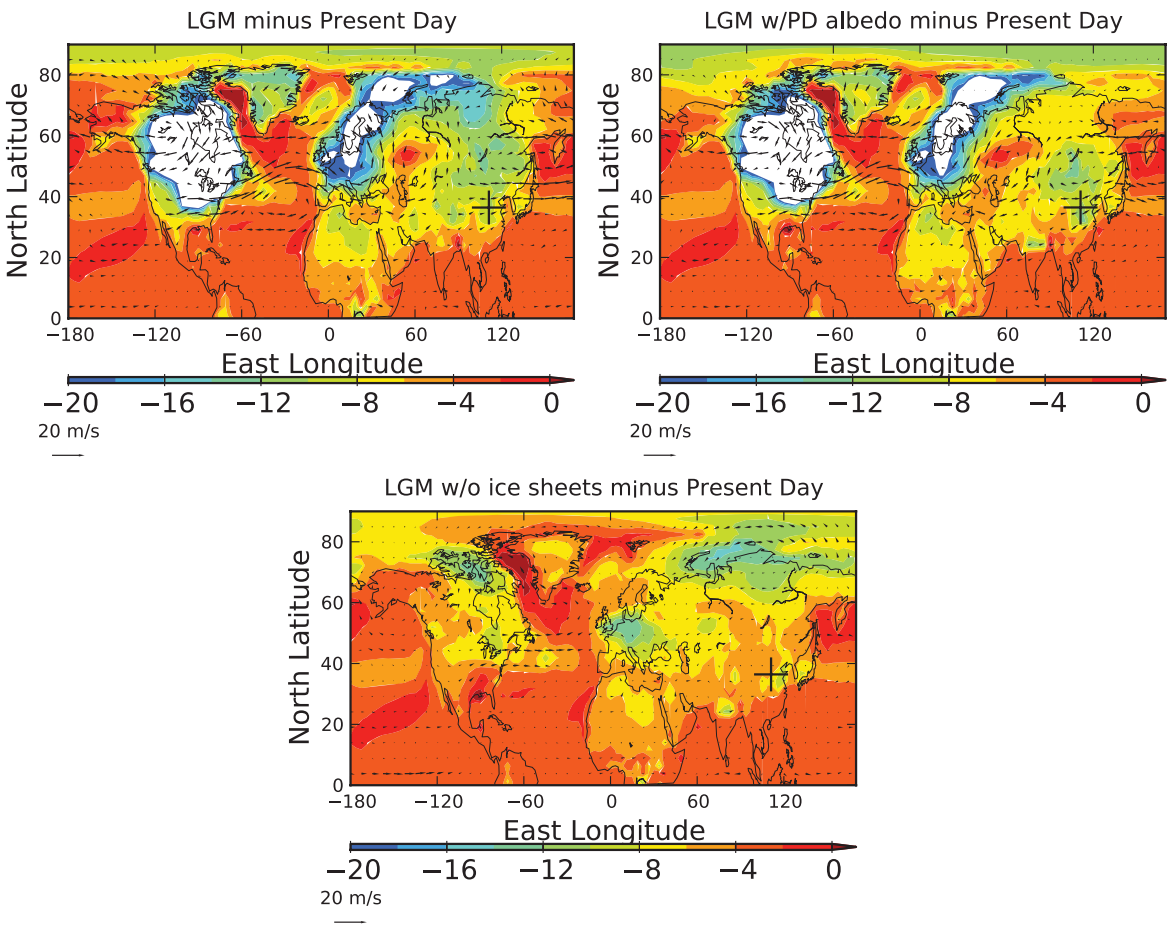

Fig. S9: Last Glacial Maximum minus Present Day surface temperature (colors) and 500-hPa wind (arrows) anomalies for test cases of the LMDZ model.

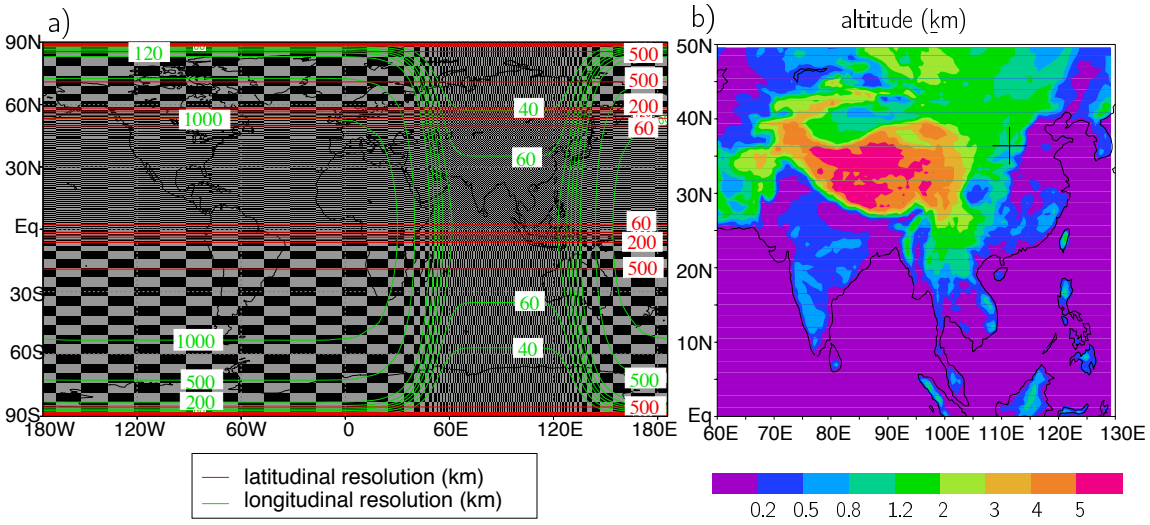

Fig. S10: Resolution of new LMDZ simulations. a) zoom configuration showing the latitudinal and longitudinal resolution. b) topography in the zoomed simulation.

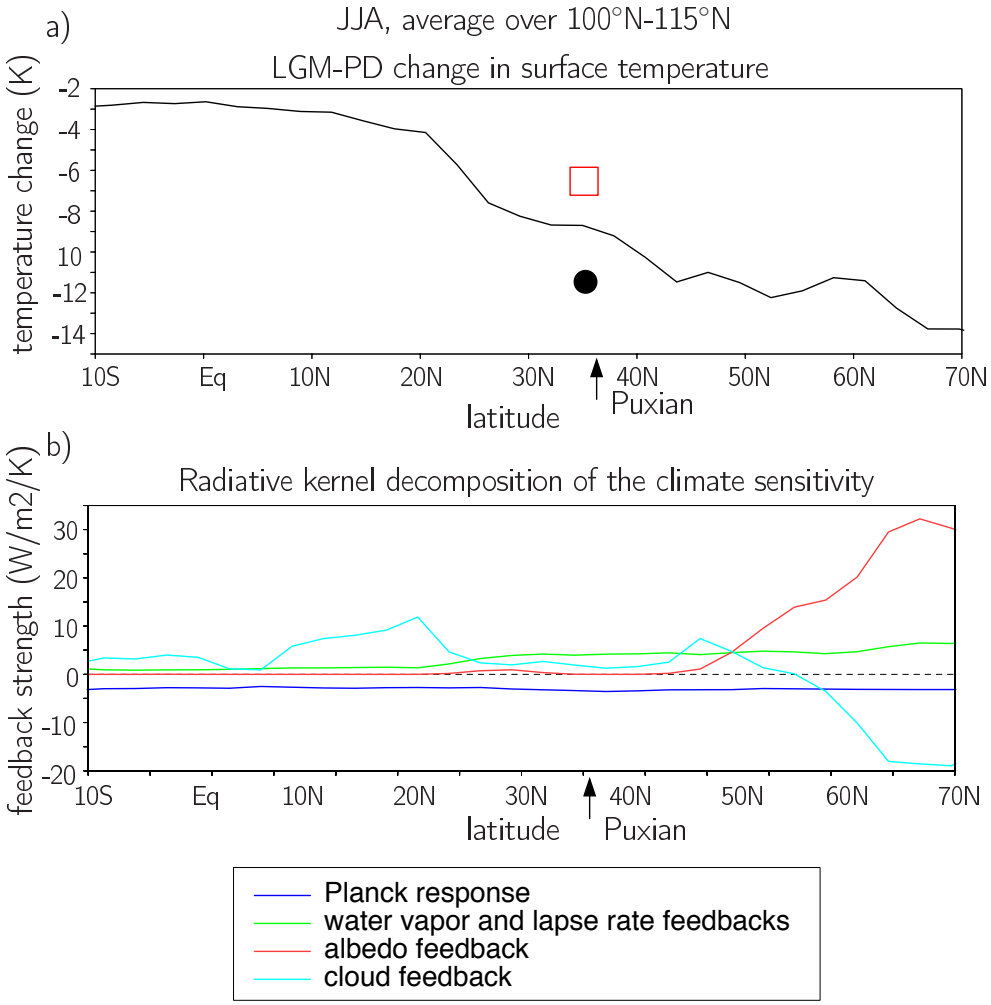

Fig. S11: Simulation of changes in temperature and feedbacks resulting in simulated regional climate sensitivity with LMDZ. a) Simulated change in mean annual surface temperature as a function of latitude, in average over 100°E-115°E (around the longitude of Puxian). The simulated and reconstructed temperature changes at Puxian are indicated by the black dot and red square respectively. b) Radiative kernel decomposition of the climate sensitivity into contributions from different feedbacks, as a function of latitude, in annual mean and in average over 100°E-115°E. Each feedback is quantified by the effect of surface temperature change on top-of-the-atmosphere radiation changes. The Planck response (blue) is the negative feedback associated with the reduced outgoing longwave radiation as the the surface cools at Last Glacial Maximum; the water vapor feedback is the positive feedback associated with the decease in water vapor as the air cools; the lapse-rate feedback is the negative feedback associated with the amplified cooling of the upper-troposphere as the surface cools; the cloud feedbacks are associated with changes in cloud cover and of their radiative properties; and the surface albedo feedback is associated with changes in snow cover.

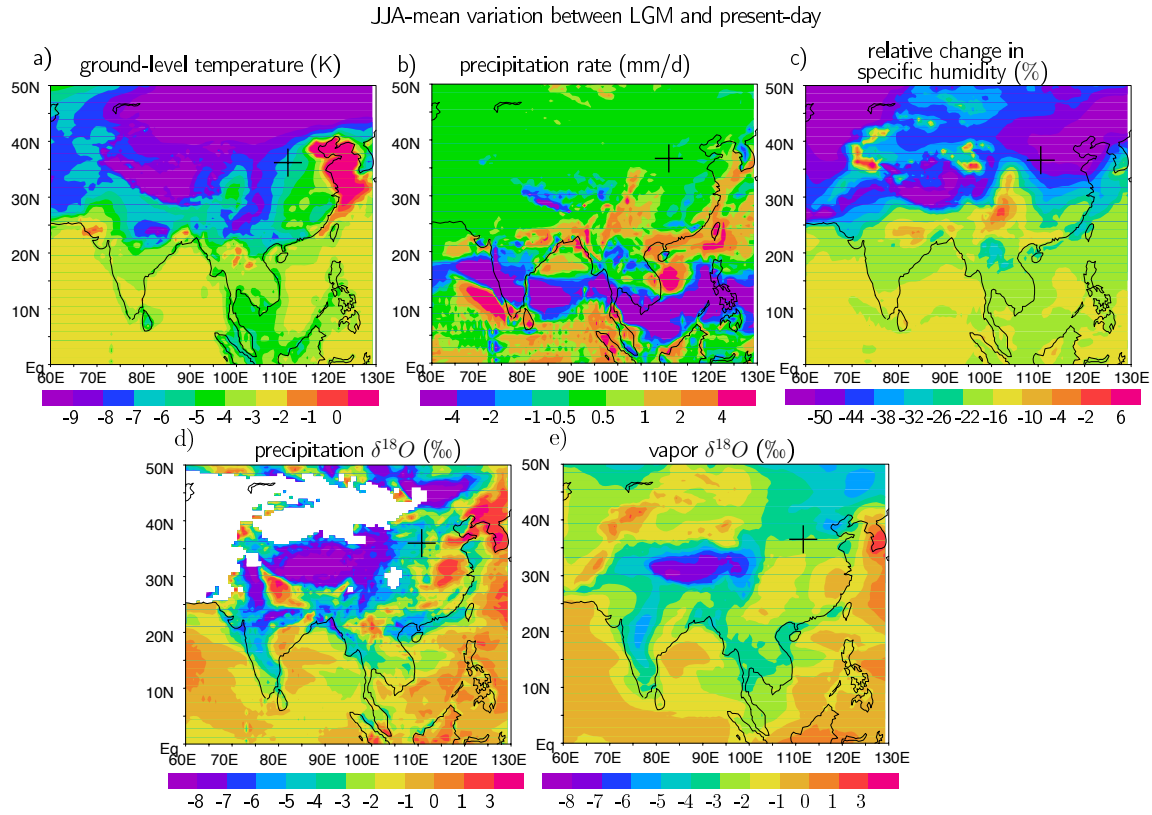

Fig. S12: Simulated changes from present to Last Glacial Maximum in temperature, precipitation, and $\delta^{18}O$. Panels show results for (a) mean JJASON (summer and autumn) ground-level temperature, (b) precipitation rate for the same time, and (c) relative change in mean annual specific humidity. Also shown is (d) changes in precipitation $\delta^{18}O$ (e) ground-level vapor $\delta^{18}O$. Puxian is indicated by the black cross.

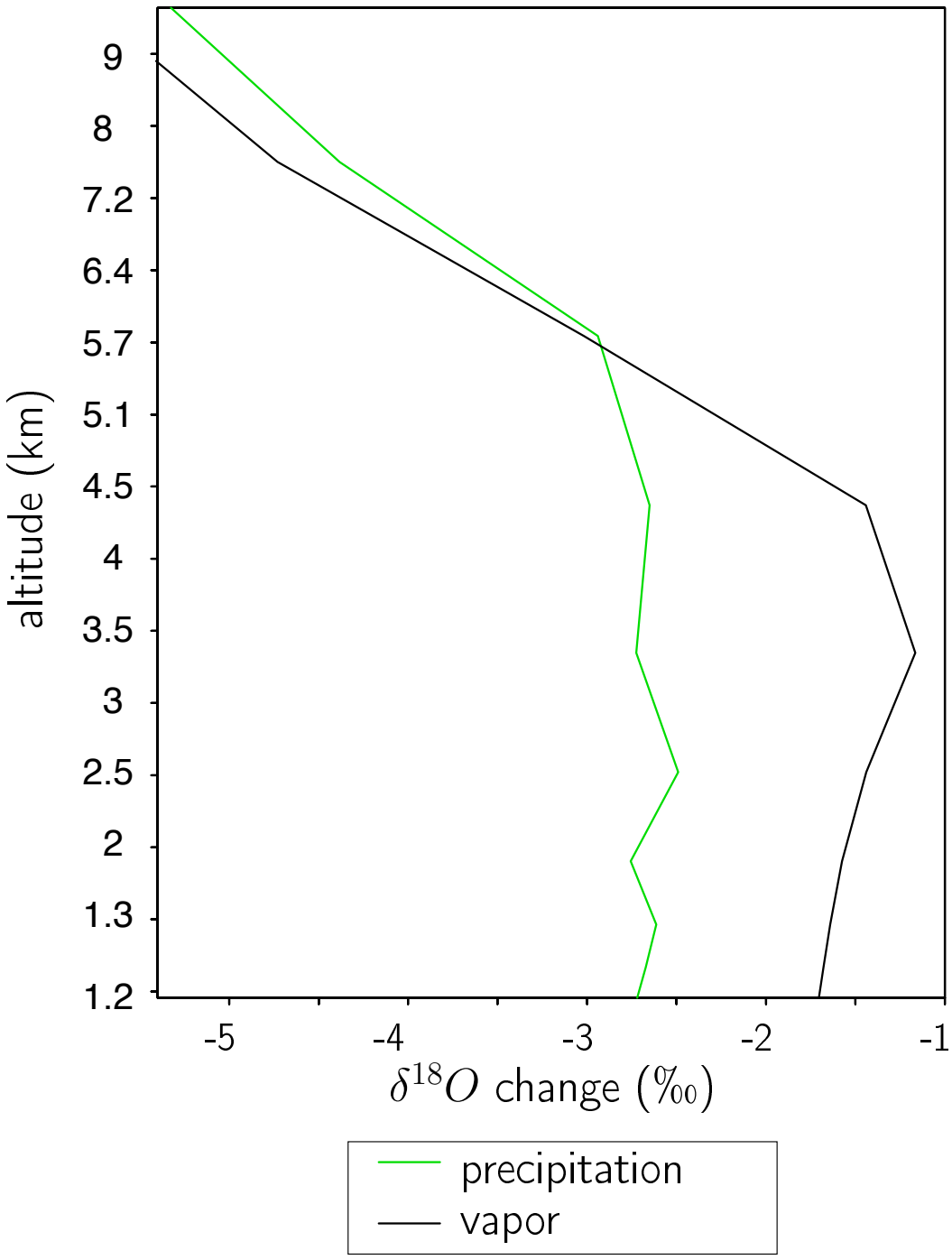

Fig. S13: Simulated vertical profile of $\delta^{18}O$ at site from LMDZ Model. Shown are outputs for vapor (black) and precipitation (green) $\delta^{18}O$ over Puxian in average for JJA.

Table S1. Average stable isotope data for all glacial and modern samples from Puxian.

Sample	Number of Specimens Analyzed	$\delta^{13}C_{mineral}$ ‰ V-PDB	$\delta^{18}O_{mineral}$ ‰ V-SMOW	Δ_{47} ‰	Δ_{47} derived Temperature °C	$\delta^{18}O_{water}$ ‰, V-SMOW	Ice volume corrected[1] $\delta^{18}O_{water}$ ‰, V-SMOW
Modern Gastropod	32	-7.1 ± 0.3	27.5 ± 0.7	0.619 ± 0.006	31.2 ± 1.5	-0.5 ± 0.7	-0.5 ± 0.7
Glacial Gastropod	37	-7.2 ± 0.4	25.0 ± 0.8	0.649 ± 0.008	24.2 ± 1.9	-4.3 ± 0.9	-5.5 ± 0.9
Glacial Soil Nodule	9	-5.1 ± 0.1	21.9 ± 0.1	0.679 ± 0.010	17.8 ± 2.0	-7.9 ± 0.5	-9.1 ± 0.5

[1]Corrected for 1.2‰ enrichment in ocean water due to the increase in global ice volume at the LGM.
± Values are two standard errors. In the case of water isotopes this is the propagated error taking into account errors in both mineral $\delta^{18}O$ and temperature determinations (SI text).

Table S2. Average stable isotope measurements for individual specimens

Sample ID[a]	No. of Analyses[b]	$\delta^{13}C$ (‰, V-PDB)	$\delta^{18}O$ (‰, V-SMOW)	Δ_{47} (‰)	Δ_{47} derived temperature (°C) [c]	$\delta^{18}O_{water}$ (‰, V-SMOW)[d]
M1	2	-8.9	27.3	0.636 ± 0.009	27.3 ± 2.1	-1.5 ± 0.5
M2	2	-8.2	28.1	0.587 ± 0.010	39.3 ± 2.6	1.6 ± 0.8
M3	2	-6.8	27.7	0.603 ± 0.029	35.1 ± 7.0	0.5 ± 1.9
M4	1	-7.4	30.6	0.623 ± 0.011	30.4 ± 2.5	2.4 ± 0.7
M5	1	-8.8	29.4	0.605 ± 0.011	34.7 ± 2.6	2.1 ± 0.7
M6	1	-7.7	30.1	0.619 ± 0.014	31.3 ± 3.2	2.1 ± 0.8
M7	1	-6.7	30.9	0.628 ± 0.013	29.1 ± 3.0	2.4 ± 0.8
M8	1	-5.0	24.6	0.617 ± 0.012	31.7 ± 2.8	-3.2 ± 0.7
M9	1	-7.8	28.0	0.622 ± 0.007	30.5 ± 1.7	-0.1 ± 0.4
M10	1	-7.6	26.4	0.648 ± 0.010	24.6 ± 2.3	-2.8 ± 0.6
M11	1	-6.2	24.9	0.635 ± 0.008	27.6 ± 1.9	-3.7 ± 0.5
M12	3	-7.5	29.3	0.589 ± 0.012	38.6 ± 3.1	2.7 ± 0.8
M13	1	-8.5	29.7	0.638 ± 0.010	26.7 ± 2.2	0.8 ± 0.6
M14	1	-6.8	26.5	0.608 ± 0.010	34.0 ± 2.4	-0.9 ± 0.6
M15	2	-6.8	27.4	0.599 ± 0.009	36.2 ± 2.3	0.4 ± 0.7
M16	1	-6.9	29.3	0.626 ± 0.013	29.5 ± 3.0	0.9 ± 0.8
M17	1	-8.0	26.9	0.624 ± 0.007	30.0 ± 1.6	-1.3 ± 0.4
M18	1	-7.7	26.9	0.624 ± 0.011	30.1 ± 2.5	-1.3 ± 0.6
M19	1	-6.1	23.2	0.623 ± 0.021	30.3 ± 4.9	-4.8 ± 1.3
M20	1	-6.8	28.7	0.613 ± 0.011	32.7 ± 2.6	0.9 ± 0.7
M21	1	-5.6	27.5	0.640 ± 0.010	26.2 ± 2.2	-1.4 ± 0.6
M22	1	-8.0	27.1	0.600 ± 0.011	35.8 ± 2.7	0.0 ± 0.7
M23	1	-7.1	26.2	0.613 ± 0.013	32.8 ± 3.1	-1.5 ± 0.8

Table S2. Average stable isotope measurements for individual specimens

Sample ID[a]	No. of Analyses[b]	$\delta^{13}C$ (‰, V-PDB)	$\delta^{18}O$ (‰, V-SMOW)	Δ_{47} (‰)	Δ_{47} derived temperature (°C) [c]	$\delta^{18}O_{water}$ (‰, V-SMOW)[d]
M24	1	-5.6	26.5	0.622 ± 0.013	30.6 ± 3.0	-1.5 ± 0.8
M25	1	-8.0	29.7	0.633 ± 0.014	27.9 ± 3.1	1.0 ± 1.1
M26	1	-7.1	26.6	0.590 ± 0.016	38.4 ± 4.1	0.0 ± 0.4
M27	1	-6.8	29.2	0.636 ± 0.006	27.3 ± 1.4	0.4 ± 0.4
M28	1	-7.8	28.6	0.610 ± 0.006	33.4 ± 1.5	1.0 ± 0.8
M29	1	-6.9	23.9	0.607 ± 0.012	34.0 ± 3.0	-3.4 ± 0.8
M30	1	-7.5	27.9	0.614 ± 0.013	32.5 ± 3.1	0.1 ± 0.8
M31	1	-4.9	26.5	0.637 ± 0.015	27.1 ± 3.5	-2.2 ± 0.9
M32	1	-5.9	24.7	0.613 ± 0.010	32.7 ± 2.5	-2.9 ± 0.6
G1	1	-5.4	24.9	0.653 ± 0.014	23.5 ± 3.0	-4.6 ± 0.8
G2	1	-6.9	27.2	0.634 ± 0.012	27.8 ± 2.7	-1.4 ± 0.7
G3	1	-7.0	27.4	0.615 ± 0.011	32.1 ± 2.6	-0.4 ± 0.7
G4	1	-7.7	24.0	0.640 ± 0.009	26.4 ± 1.9	-4.8 ± 0.5
G5	1	-7.6	23.8	0.626 ± 0.011	29.6 ± 2.6	-4.4 ± 0.7
G6	1	-8.2	23.2	0.666 ± 0.013	20.6 ± 2.7	-6.8 ± 0.7
G7	1	-8.2	23.2	0.687 ± 0.008	16.3 ± 1.7	-7.6 ± 0.4
G8	1	-8.4	27.4	0.633 ± 0.009	27.8 ± 2.1	-1.3 ± 0.5
G9	1	-8.4	27.5	0.599 ± 0.011	36.2 ± 2.8	0.5 ± 0.7
G10	2	-7.0	21.7	0.685 ± 0.005	16.6 ± 1.0	-9.0 ± 0.3
G11	1	-8.3	21.1	0.673 ± 0.012	19.0 ± 2.5	-9.1 ± 0.7

Table S2. Average stable isotope measurements for individual specimens

Sample ID[a]	No. of Analyses[b]	$\delta^{13}C$ (‰, V-PDB)	$\delta^{18}O$ (‰, V-SMOW)	Δ_{47} (‰)	Δ_{47} derived temperature (°C)[c]	$\delta^{18}O_{water}$ (‰, V-SMOW)[d]
G12	1	-6.0	27.9	0.672 ± 0.011	19.4 ± 2.2	-2.5 ± 0.6
G13	1	-6.7	27.5	0.690 ± 0.007	15.6 ± 1.5	-3.6 ± 0.4
G14	1	-6.1	26.5	0.702 ± 0.008	13.1 ± 1.6	-5.2 ± 0.4
G15	2	-6.9	22.1	0.656 ± 0.022	22.8 ± 4.8	-7.4 ± 1.3
G16	1	-5.9	26.4	0.673 ± 0.012	19.2 ± 2.5	-3.9 ± 0.7
G17	2	-10.0	26.9	0.653 ± 0.012	23.4 ± 2.6	-2.6 ± 0.7
G18	2	-6.8	20.9	0.671 ± 0.010	19.6 ± 2.1	-9.2 ± 0.5
G19	1	-7.0	24.7	0.654 ± 0.016	23.1 ± 3.4	-4.8 ± 0.9
G20	1	-7.8	23.4	0.646 ± 0.013	25.0 ± 2.9	-5.7 ± 0.7
G21	1	-8.4	23.1	0.624 ± 0.012	30.1 ± 2.8	-5.0 ± 0.7
G22	1	-4.5	23.1	0.626 ± 0.015	29.5 ± 3.5	-5.1 ± 0.9
G23	1	-7.3	21.3	0.656 ± 0.011	22.8 ± 2.4	-8.1 ± 0.6
G24	1	-9.8	26.2	0.640 ± 0.021	26.2 ± 4.6	-2.7 ± 1.2
G25	1	-7.3	28.0	0.656 ± 0.012	22.9 ± 2.6	-1.6 ± 0.7
G26	2	-6.8	20.9	0.671 ± 0.010	19.6 ± 2.1	-9.2 ± 0.5
G27	2	-6.9	26.5	0.613 ± 0.015	32.8 ± 3.6	-1.1 ± 0.9
G28	2	-5.9	25.6	0.629 ± 0.002	29.0 ± 0.5	-2.8 ± 0.1
G29	2	-7.5	24.5	0.624 ± 0.032	30.1 ± 7.3	-3.7 ± 1.9
G30	3	-7.9	22.6	0.619 ± 0.007	31.2 ± 1.8	-5.2 ± 0.5
G31	2	-6.5	27.6	0.637 ± 0.001	26.9 ± 0.2	-1.3 ± 0.1
G32	1	-5.9	25.9	0.669 ± 0.015	20.0 ± 3.1	-4.2 ± 0.8
G33	1	-5.9	25.7	0.646 ± 0.013	25.0 ± 2.6	-3.4 ± 0.7

Table S2. Average stable isotope measurements for individual specimens

Sample ID[a]	No. of Analyses[b]	$\delta^{13}C$ (‰, V-PDB)	$\delta^{18}O$ (‰, V-SMOW)	Δ_{47} (‰)	Δ_{47} derived temperature (°C)[c]	$\delta^{18}O_{water}$ (‰, V-SMOW)[d]
G34	2	-7.6	24.7	0.636 ± 0.011	27.2 ± 2.8	-4.0 ± 1.6
G35	2	-7.5	28.1	0.648 ± 0.012	24.5 ± 2.6	-1.3 ± 0.7
G36	1	-7.6	28.0	0.641 ± 0.011	26.1 ± 2.5	-1.0 ± 0.6
G37	2	-6.8	23.8	0.666 ± 0.010	20.5 ± 2.0	-6.2 ± 1.6
GSN1	1	-4.9	21.8	0.680 ± 0.009	17.6 ± 1.9	-8.0 ± 0.4
GSN2	1	-4.9	21.8	0.675 ± 0.013	18.6 ± 2.9	-7.8 ± 0.6
GSN3	1	-5.2	22.0	0.675 ± 0.019	18.8 ± 4.2	-7.6 ± 0.9
GSN4	1	-5.2	22.1	0.712 ± 0.010	11.2 ± 2.0	-9.1 ± 0.4
GSN5	1	-5.2	21.8	0.659 ± 0.009	22.1 ± 2.0	-7.1 ± 0.4
GSN6	1	-5.2	21.9	0.683 ± 0.020	17.0 ± 4.2	-8.0 ± 0.9
GSN7	1	-5.0	21.9	0.682 ± 0.012	17.3 ± 2.5	-8.0 ± 0.9
GSN8	1	-5.1	21.9	0.689 ± 0.011	15.8 ± 2.3	-8.3 ± 0.5
GSN9	1	-5.3	21.9	0.659 ± 0.009	22.1 ± 2.0	-6.9 ± 0.4
MSN	3	-0.5	24.0	0.676 ± 0.007	18.6 ± 0.8	-5.7 ± 0.3

[a] M represents modern gastropod specimens, G represents glacial gastropod. GSN represents glacial soil nodule, MSN represents a modern soil nodule from the Badain Jaran Desert.

[b] Number of distinct extractions of CO_2 gas from a sample analyzed for stable isotopes.

[c] Calculated using the calibration line of Ghosh et al., 2006.

[d] Calculated using the Δ_{47} derived temperature and the equation for $\delta^{18}O$ fractionation between aragonite or calcite and water described in the SI Text.

± Δ_{47}, ± values represent the precision of the measurement to one standard error, in this case either the average and standard error of analyses for distinct extractions of CO_2 the same specimen, or if only one analysis was performed it represents the internal error of the

measurement. If two replicate analysis were conducted then the error estimates values represent the standard deviation, not the standard error. ± $\delta^{18}O_{water}$ values are propagated errors (1 s.e.) taking into account errors in both $\delta^{18}O_{carbonate}$ and Δ_{47} temperature determinations.

Table S3. Raw δ_{47} and Δ_{47} data with corrections in analytical sequence

Sequence Number[a]	Type	Date	Sample ID	δ_{47} raw ‰, WG	Δ_{47} raw ‰, WG	HG Slope	HG Intercept	Δ_{47} unstretched[a] ‰, HG	Δ_{47} stretched[b] ‰, HG	Δ_{47} acid[c] ‰, HG	Δ_{47} accepted[d] ‰, HG	Δ_{47} residual[e] ‰
Data Obtained on Caltech Mass Spectrometer 1												
1	Standard	3/24/10	Carmel Chalk	11.325	-0.255	0.004	-0.841	0.541	0.543	0.623	0.644	-0.021
2	Standard	3/24/10	Carrara Marble	17.706	-0.451	0.004	-0.841	0.319	0.320	0.400	0.352	0.048
3	Sample	3/24/10	MSN	10.138	-0.204	0.004	-0.841	0.596	0.599	0.679		
4	Standard	3/24/10	Carmel Chalk	11.254	-0.233	0.004	-0.841	0.563	0.566	0.646	0.644	0.002
5	Sample	3/24/10	MSN	10.081	-0.221	0.004	-0.841	0.580	0.583	0.663		
6	Standard	3/24/10	Carrara Marble	17.595	-0.471	0.004	-0.841	0.301	0.302	0.382	0.352	0.03
7	Standard	11/19/10	Carmel Chalk	11.523	-0.126	0.014	-0.807	0.521	0.546	0.626	0.644	-0.018
8	Sample	11/19/10	G3	7.616	-0.190	0.014	-0.807	0.511	0.535	0.615		
9	Sample	11/20/10	G4	3.587	-0.223	0.014	-0.807	0.534	0.560	0.640		
10	Sample	11/20/10	G9	6.323	-0.224	0.014	-0.807	0.495	0.519	0.599		
11	Sample	11/20/10	G6	2.191	-0.217	0.014	-0.807	0.560	0.586	0.666		
12	Sample	11/20/10	G10	2.063	-0.187	0.014	-0.807	0.591	0.619	0.699		
13	Sample	11/20/10	M5	7.921	-0.196	0.014	-0.807	0.501	0.525	0.605		
14	Sample	11/20/10	M6	9.658	-0.159	0.014	-0.807	0.514	0.539	0.619		
15	Standard	11/20/10	Carmel Chalk	11.455	-0.126	0.014	-0.807	0.522	0.547	0.627	0.644	-0.017
16	sample	11/20/10	M7	11.419	-0.125	0.014	-0.807	0.523	0.548	0.628		
17	Standard	11/23/10	Carrara Marble	17.942	-0.291	0.014	-0.807	0.267	0.280	0.360	0.352	0.008
18	Sample	11/23/10	M9	7.504	-0.185	0.014	-0.807	0.517	0.542	0.622		
19	Sample	11/23/10	G19	4.977	-0.189	0.014	-0.807	0.549	0.574	0.654		
20	Sample	11/23/10	M16	9.642	-0.151	0.014	-0.807	0.522	0.546	0.626		
21	Sample	11/23/10	M15	8.105	-0.210	0.014	-0.807	0.485	0.507	0.587		
22	Sample	11/23/10	M14	6.919	-0.207	0.014	-0.807	0.504	0.528	0.608		
23	Sample	11/23/10	M13	8.508	-0.156	0.014	-0.807	0.533	0.558	0.638		
24	Sample	11/23/10	M12	9.018	-0.206	0.014	-0.807	0.476	0.499	0.579		
25	Standard	11/24/10	Carmel Chalk	11.490	-0.111	0.014	-0.807	0.537	0.562	0.642	0.644	-0.002
26	Sample	11/24/10	G21	1.937	-0.261	0.014	-0.807	0.519	0.544	0.624		
27	Sample	11/24/10	G22	5.770	-0.205	0.014	-0.807	0.522	0.546	0.626		
28	Standard	11/24/10	Carmel Chalk	11.481	-0.129	0.014	-0.807	0.519	0.544	0.624	0.644	-0.020
29	Sample	11/25/10	M8	6.725	-0.201	0.014	-0.807	0.513	0.537	0.617		
30	Sample	11/25/10	M17	6.164	-0.202	0.014	-0.807	0.520	0.544	0.624		
31	Sample	11/25/10	M15	7.483	-0.197	0.014	-0.807	0.506	0.530	0.610		
32	Sample	11/25/10	M12	9.007	-0.186	0.014	-0.807	0.496	0.520	0.600		
33	Sample	11/25/10	G23	1.223	-0.240	0.014	-0.807	0.550	0.576	0.656		
34	Standard	11/25/10	Carrara Marble	17.919	-0.292	0.014	-0.807	0.266	0.279	0.359	0.352	0.007
35	Sample	11/25/10	G24	3.694	-0.221	0.014	-0.807	0.535	0.560	0.640		
36	Sample	11/25/10	G25	8.024	-0.146	0.014	-0.807	0.550	0.576	0.656		
37	Sample	11/26/10	G26	6.979	-0.222	0.014	-0.807	0.488	0.511	0.591		
38	Standard	12/1/10	Carrara Marble	17.902	-0.303	0.014	-0.807	0.255	0.267	0.347	0.352	-0.005
39	Standard	12/1/10	NBS-19	17.197	-0.319	0.014	-0.807	0.249	0.261	0.341	0.352	-0.011
40	Sample	12/2/10	G26	3.578	-0.201	0.014	-0.807	0.556	0.582	0.662		
41	Sample	12/2/10	G27	6.889	-0.213	0.014	-0.807	0.498	0.522	0.602		
42	Sample	12/2/10	G28	6.896	-0.189	0.014	-0.807	0.522	0.547	0.627		
43	Sample	12/2/10	G29	4.259	-0.208	0.014	-0.807	0.540	0.566	0.646		
44	Standard	12/2/10	NBS-19	17.170	-0.292	0.014	-0.807	0.277	0.290	0.370	0.352	0.018
45	Sample	12/2/10	M12	9.130	-0.162	0.014	-0.807	0.518	0.542	0.622		
46	Sample	12/2/10	G30	1.867	-0.263	0.014	-0.807	0.519	0.543	0.623		
47	Sample	12/3/10	G31	8.402	-0.157	0.014	-0.807	0.534	0.559	0.639		
48	Sample	12/3/10	G34	5.270	-0.224	0.014	-0.807	0.510	0.534	0.614		
49	Sample	12/3/10	G35	7.848	-0.163	0.014	-0.807	0.535	0.560	0.640		
50	Sample	12/3/10	G37	3.431	-0.195	0.014	-0.807	0.565	0.592	0.672		
51	Standard	12/4/10	Carrara Marble	17.804	-0.286	0.014	-0.807	0.274	0.287	0.367	0.352	0.015
52	Sample	12/4/10	G27	6.914	-0.192	0.014	-0.807	0.519	0.544	0.624		

53	Sample	12/4/10	G28	6.845	-0.186	0.014	-0.807	0.526	0.550	0.630		
54	Sample	12/4/10	G29	4.006	-0.253	0.014	-0.807	0.498	0.522	0.602		
55	Sample	12/5/10	G30	1.878	-0.279	0.014	-0.807	0.503	0.526	0.606		
56	Sample	12/5/10	G32	7.316	-0.143	0.014	-0.807	0.563	0.589	0.669		
57	Standard	12/5/10	Carmel Chalk	11.365	-0.114	0.014	-0.807	0.536	0.561	0.641	0.644	-0.003
58	Sample	12/5/10	G33	7.021	-0.169	0.014	-0.807	0.540	0.566	0.646		
59	Sample	12/5/10	G34	3.383	-0.208	0.014	-0.807	0.552	0.578	0.658		
60	Sample	12/5/10	G36	7.688	-0.165	0.014	-0.807	0.536	0.561	0.641		
61	Sample	12/5/10	G37	5.101	-0.181	0.014	-0.807	0.555	0.581	0.661		
62	Standard	12/6/10	Carrara Marble	17.897	-0.268	0.014	-0.807	0.291	0.305	0.385	0.352	0.033
63	Sample	12/9/10	G30	1.936	-0.253	0.014	-0.807	0.526	0.552	0.632		
64	Sample	12/9/10	G31	8.299	-0.158	0.014	-0.807	0.531	0.556	0.636		
65	Sample	12/10/10	G35	7.768	-0.146	0.014	-0.807	0.550	0.576	0.656		
66	Sample	12/10/10	M18	6.441	-0.196	0.014	-0.807	0.519	0.544	0.624		
67	Sample	12/10/10	M19	4.315	-0.227	0.014	-0.807	0.518	0.543	0.623		
68	Sample	12/10/10	M20	9.077	-0.169	0.014	-0.807	0.508	0.533	0.613		
69	Standard	12/10/10	Carmel Chalk	11.383	-0.106	0.014	-0.807	0.539	0.565	0.645	0.644	0.001
70	Sample	12/10/10	M21	8.550	-0.150	0.014	-0.807	0.535	0.560	0.640		
71	Sample	12/10/10	M22	6.856	-0.213	0.014	-0.807	0.497	0.520	0.600		
72	Sample	12/10/10	M23	6.580	-0.205	0.014	-0.807	0.508	0.533	0.613		
73	Sample	12/11/10	M24	8.163	-0.174	0.014	-0.807	0.517	0.542	0.622		
74	Sample	12/11/10	M25	8.985	-0.151	0.014	-0.807	0.528	0.553	0.633		
75	Standard	12/11/10	Carrara Marble	17.850	-0.261	0.014	-0.807	0.292	0.306	0.386	0.352	0.034
76	Sample	12/11/10	M26	6.682	-0.225	0.014	-0.807	0.487	0.510	0.590		
77	Sample	12/11/10	M27	9.666	-0.139	0.014	-0.807	0.531	0.556	0.636		
78	Sample	12/13/10	M28	8.065	-0.187	0.014	-0.807	0.506	0.530	0.610		
79	Sample	12/13/10	M29	4.224	-0.243	0.014	-0.807	0.503	0.527	0.607		
80	Sample	12/14/10	M30	7.603	-0.189	0.014	-0.807	0.509	0.534	0.614		
81	Sample	12/14/10	M31	8.805	-0.150	0.014	-0.807	0.531	0.557	0.637		
82	Sample	12/14/10	M32	5.938	-0.214	0.014	-0.807	0.509	0.533	0.613		
83	Standard	2/7/12	Carrara Marble	17.831	-0.2697	0.013	-0.721	0.217	0.255	0.335	0.352	-0.017
84	Sample	2/8/12	GSN5	3.416	-0.1984	0.013	-0.721	0.477	0.560	0.659		
85	Standard	2/8/12	TV01	11.233	-0.113	0.013	-0.721	0.460	0.540	0.620	0.662	-0.042
86	Sample	2/8/12	GSN6	3.577	-0.1594	0.013	-0.721	0.514	0.603	0.683		
87	Sample	2/8/12	GSN7	3.743	-0.1586	0.013	-0.721	0.513	0.602	0.682		
88	Sample	2/9/12	GSN8	3.637	-0.1537	0.013	-0.721	0.519	0.609	0.689		
89	Standard	2/9/12	Carrara Marble	17.830	-0.2675	0.013	-0.721	0.220	0.258	0.338	0.352	-0.014
90	Sample	2/9/12	GSN9	3.496	-0.1813	0.013	-0.721	0.494	0.579	0.659		

Data Obtained on Caltech Mass Spectrometer 2

1	Standard	10/15/10	102-GC-AZ01	3.149	-0.189	0.020	-0.772	0.520	0.569	0.649	0.657	-0.008
2	Sample	10/15/10	G12	9.252	-0.046	0.020	-0.772	0.540	0.592	0.672		
3	Sample	10/19/10	G2	7.593	-0.126	0.020	-0.801	0.524	0.554	0.634		
4	Standard	10/19/10	Carrara Marble	17.468	-0.148	0.020	-0.801	0.306	0.323	0.403	0.352	0.051
5	Sample	10/19/10	G5	3.319	-0.218	0.020	-0.801	0.517	0.546	0.626		
6	Sample	10/19/10	M1	5.797	-0.162	0.020	-0.801	0.524	0.553	0.633		
7	Sample	10/19/10	G6	6.262	-0.152	0.020	-0.801	0.524	0.553	0.633		
8	Standard	10/20/10	102-GC-AZ01	3.221	-0.158	0.020	-0.801	0.579	0.611	0.691	0.657	0.034
9	Standard	10/21/10	102-GC-AZ01	2.933	-0.184	0.020	-0.801	0.559	0.590	0.670	0.657	0.013
10	Sample	11/16/10	G13	8.157	-0.051	0.020	-0.772	0.557	0.610	0.690		
11	Sample	11/16/10	G14	7.762	-0.048	0.020	-0.772	0.568	0.622	0.702		
12	Sample	2010-17-11	G11	0.020	-0.230	0.020	-0.772	0.542	0.593	0.673		
13	Sample	2010-17-11	M1	5.647	-0.149	0.020	-0.772	0.510	0.558	0.638		
14	Sample	2010-17-11	G1	6.712	-0.114	0.020	-0.772	0.523	0.573	0.653		
15	Standard	2010-18-11	Carrara Marble	17.964	-0.173	0.020	-0.772	0.240	0.263	0.343	0.352	-0.009
16	Standard	2010-18-11	102-GC-AZ01	3.221	-0.189	0.020	-0.772	0.519	0.568	0.648	0.657	-0.009
17	Sample	2010-18-11	G7	2.300	-0.172	0.020	-0.772	0.554	0.607	0.687		
18	Sample	2010-19-11	G10	1.883	-0.194	0.020	-0.772	0.540	0.592	0.672		
19	Standard	2010-19-11	Carmel Chalk	11.449	-0.047	0.020	-0.772	0.496	0.543	0.623	0.644	-0.021
20	Standard	2010-19-11	G15	2.185	-0.214	0.020	-0.772	0.514	0.563	0.643		
21	Sample	2010-19-11	G16	7.801	-0.075	0.020	-0.772	0.541	0.593	0.673		
22	Sample	2010-20-11	G17	4.249	-0.173	0.020	-0.772	0.514	0.563	0.643		
23	Sample	2010-20-11	G18	1.304	-0.213	0.020	-0.772	0.532	0.583	0.663		

24	Standard	2010-20-11	Carmel Chalk	11.543	-0.034	0.020	-0.772	0.507	0.555	0.635	0.644	-0.009
25	Standard	2010-21-11	Carrara Marble	17.984	-0.169	0.020	-0.772	0.243	0.266	0.346	0.352	-0.006
26	Sample	2010-23-11	M2	7.435	-0.160	0.020	-0.772	0.463	0.508	0.588		
27	Sample	2010-22-11	M3	7.731	-0.151	0.020	-0.772	0.466	0.510	0.590		
28	Sample	2010-23-11	M4	10.562	-0.065	0.020	-0.772	0.495	0.543	0.623		
29	Standard	2010-23-11	Carrara Marble	17.942	-0.184	0.020	-0.772	0.229	0.251	0.331	0.352	-0.021
30	sample	2010-11-23	M10	6.126	-0.131	0.020	-0.772	0.518	0.568	0.648		
31	sample	2010-11-24	G20	2.855	-0.198	0.020	-0.772	0.517	0.566	0.646		
32	sample	2010-11-24	M11	5.906	-0.147	0.020	-0.772	0.506	0.555	0.635		
33	Standard	2010-11-24	Carmel Chalk	11.485	-0.047	0.020	-0.772	0.495	0.542	0.622	0.644	-0.022
34	Sample	2010-11-24	M2	6.802	-0.174	0.020	-0.772	0.461	0.505	0.585		
35	Sample	2010-11-24	M3	8.616	-0.110	0.020	-0.772	0.489	0.536	0.616		
36	Sample	2010-11-25	G15	2.538	-0.183	0.020	-0.772	0.538	0.589	0.669		
37	Standard	2010-11-25	Carrara Marble	17.949	-0.139	0.020	-0.772	0.274	0.300	0.380	0.352	0.028
38	Sample	2010-11-25	G17	4.129	-0.156	0.020	-0.772	0.533	0.584	0.664		
39	Sample	2010-11-25	G18	1.294	-0.199	0.020	-0.772	0.546	0.599	0.679		
40	Standard	2010-11-26	Carmel Chalk	11.463	-0.027	0.020	-0.772	0.516	0.565	0.645	0.644	0.001
41	Standard	02/08/12	Carrara Marble	17.599	-0.500	0.005	-0.849	0.254	0.253	0.333	0.352	-0.019
42	Sample	02/08/12	GSN1	3.663	-0.226	0.005	-0.849	0.603	0.600	0.680		
43	Sample	02/09/12	GSN2	3.605	-0.232	0.005	-0.849	0.598	0.595	0.675		
44	Standard	02/09/12	Carrara Marble	17.665	-0.534	0.005	-0.849	0.220	0.219	0.299	0.352	-0.053
45	Sample	02/09/12	GSN3	3.535	-0.233	0.005	-0.849	0.597	0.595	0.675		
46	Sample	02/09/12	GSN4	3.742	-0.194	0.005	-0.849	0.635	0.632	0.712		
47	Standard	02/10/12	TV01	11.160	-0.203	0.005	-0.849	0.586	0.583	0.663	0.662	0.001

WG: Working gas (Oztech)
HG: Heated gas

[a] Corrected versus the heated gas reference frame (Eiler and Schauble, 2004; Affek et al., 2006).
[b] Corrected for instrument nonlinearity (Affek et al., 2006).
[c] Corrected for the acid digestion temperature.
[d] Accepted value for standard, based on >40 analyses.
[e] Measured Δ_{47} - accepted Δ_{47} value.

Table S4: Elevation of GCM grid cells for Puxian from PMIP2 GCMs. OAV = ocean, atmosphere, and vegetation-enabled model; OA = ocean and atmosphere enabled model.

Model	elevation (m)
HadCM3M2 (OAV)	1120
CCSM (OA)	1154
MIROC3.2 (OA)	1164
HadCM3M2 (OA)	1120
CNRM (OA)	1276
ECBILT (OA)	1083
FGOALS (OA)	1210
IPSL (OA)	833

Table S5: LGM-Modern temperature differences at Puxian from PMIP2 GCMs.

Parameter	Model							
	HadCM3M2 (OAV)	CCSM (OA)	MIROC3.2 (OA)	HadCM3M2 (OA)	CNRM (OA)	ECBILT (OA)	FGOALS (OA)	IPSL (OA)
JJA 2m Air Temperature[1]	-5.0	-3.1	-2.7	-3.4	-2.8	-0.1	-3.6	-5.7
DJF 2m Air Temperature[1]	-7.2	-3.5	-3.4	-3.8	-3.1	-3.8	2.0	-5.6
Annual 2m Air Temperature[1]	-5.4	-3.3	-3.0	-3.4	-3.3	-2.9	-1.9	-5.8
JJA Surface Skin Temperature[2]	-4.3	-3.1	-2.9	-3.2	-2.9	0.1	-3.1	-5.6
DJF Surface Skin Temperature[2]	-7.0	-3.6	-3.5	-3.7	-2.7	-4.5	1.2	-5.7
Annual Surface Skin Temperature[2]	-4.8	-3.2	-3.1	-3.2	-3.2	-3.2	-1.8	-5.8

[1] Modeled air temperature at 2 m.
[2] Modeled temperature at the land-atmosphere boundary.
JJA = June, July, and August.
DJF = December, January, and February
OAV = Ocean, atmosphere, and vegetation enabled model.
OA = Ocean and atmosphere enabled model.
N/D = Not determined.
All temperatures are modeled modern temperatures subtracted from modeled LGM temperatures at Puxian and are given in °C.

Table S6: LGM-Modern differences in hydrologic parameters from PMIP2 GCMs.

Parameter	Model							
	HadCM3M2 (OAV)	CCSM (OA)	MIROC3.2 (OA)	HadCM3M2 (OA)	CNRM (OA)	ECBILT (OA)	FGOALS (OA)	IPSL (OA)
JJA Total Precipitation[1]	-1.8×10^{-5}	-1.2×10^{-5}	-7.8×10^{-6}	-1.9×10^{-5}	-6.8×10^{-6}	-8.8×10^{-7}	-5.5×10^{-5}	-2.8×10^{-6}
DJF Total Precipitation[1]	2.2×10^{-5}	-8.7×10^{-7}	-4.7×10^{-7}	-4.6×10^{-7}	-2.8×10^{-7}	1.4×10^{-6}	-4.3×10^{-6}	-3.3×10^{-6}
Annual Total Precipitation[1]	3.6×10^{-6}	-8.6×10^{-6}	-5.4×10^{-6}	-8.2×10^{-6}	-9.1×10^{-7}	-5.5×10^{-7}	-3.5×10^{-5}	-3.5×10^{-6}
JJA Total Surface Evaporation[2]	-1.0×10^{-6}	N/D	N/D	-9.0×10^{-6}	1.6×10^{-6}	-3.6×10^{-6}	-1.2×10^{-5}	2.5×10^{-5}
DJF Total Surface Evaporation[2]	-2.2×10^{-6}	N/D	N/D	-2.0×10^{-6}	2.7×10^{-8}	-4.5×10^{-6}	4.4×10^{-8}	9.3×10^{-6}
Annual Total Surface Evaporation[2]	-4.2×10^{-6}	N/D	N/D	-6.1×10^{-6}	-5.0×10^{-7}	-4.7×10^{-6}	2.3×10^{-6}	1.4×10^{-5}
JJA Precipitation – Evaporation	-1.7×10^{-5}	N/D	N/D	-9.7×10^{-6}	-8.4×10^{-6}	2.6×10^{-6}	-6.7×10^{-5}	-2.8×10^{-5}
DJF Precipitation – Evaporation	2.4×10^{-5}	N/D	N/D	1.6×10^{-6}	-3.1×10^{-7}	5.8×10^{-6}	-4.3×10^{-6}	-1.3×10^{-5}
Annual Precipitation – Evaporation	7.8×10^{-6}	N/D	N/D	-2.1×10^{-6}	-4.1×10^{-7}	4.2×10^{-6}	-3.7×10^{-5}	-1.8×10^{-5}

JJA = June, July, and August.
DJF = December, January, and February
OAV = Ocean, atmosphere, and vegetation enabled model.
OA = Ocean and atmosphere enabled model.
N/D = Not determined.
All numbers are kg m^{-2} s^{-1}.

Table S7: Calculated surface water $\delta^{18}O$ (i.e., precipitation $\delta^{18}O$) based on model of snail body water $\delta^{18}O$. The difference in LGM-modern $\delta^{18}O_{sbw}$ values of snail body water can be explained by changes in h_{surf}, the relative humidity of the snail habitat, or $\delta^{18}O_{surf}$, corresponding to the average $\delta^{18}O$ of local precipitation. Note: The equilibrium fractionation is expressed as coefficient: $\varepsilon_{wv} = \alpha_{wv} - 1$.

	Temp (°C)	ε_{wv} (‰)	$\delta^{18}O_{sbw}$ (‰)	h_{surf}	$\delta^{18}O_{surf}$ (‰)	$\delta^{18}O_{surf}$ LGM-modern
Modern	31.2	8.9	-0.5	0.81	-7.7	
LGM	24.2	9.4	-4.3	0.81	-11.6	-3.9
				0.76	-13.5	-5.8
				0.94	-6.5	1.2

Table S8: Hydrologic data used for snail body water model. Possible range of $\delta^{18}O_{surf}$ values for the sampling site (Puxian): mean $\delta^{18}O_{rain}$ of local summer precipitation for nearby GNIP stations (IAEA/WMO 2006), and their mean summer air temperatures (JJA). The range of summer rain $\delta^{18}O$ values results in a range of $\delta^{18}O_{surf}$ during the LGM, but the LGM-modern difference in $\delta^{18}O_{surf}$ is stable.

Sampling site:	lat	lon	alt (m)	air temp (°C) (JJA)	h_{surf}	$\delta^{18}O_{surf} = \delta^{18}O_{rain}$ (‰) (JJA)	$\delta^{18}O_{surf}$ LGM (‰)
Puxian	36.42	111.15	1148				
Nearby GNIP stations:							
Taiyuan	37.78	112.55	778	22.1	0.82	-7.1	-11.0
Xian	34.30	108.93	397	25.6	0.82	-7.2	-11.1
Zhengzhou	34.52	113.84	110	26.0	0.80	-7.8	-11.7
Shijiazhuang	38.03	114.42	80	26.9	0.81	-7.7	-11.6

Table S9

Site name	Proxy Host	Lat. (° N)	Long. (° E)	Altitude (Meters)	Proxy LGM-PD/H T (°C)	JJA Model LGM-PD/H T (°C) zLMDZ	MA Model LGM-PD/H T (°C) zLMDZ	Proxy LGM-PD/H $\delta^{18}O$ (‰)	JJA Model LGM-PD/H $\delta^{18}O$ (‰) zLMDZ	MA Model LGM-PD/H $\delta^{18}O$ (‰) zLMDZ	Reference
Puxian[1]	Gastropods	36.4	111.1	1148	-7.0	-6.7	-4.7	-5.2	-3.3	-3.6	This study
Puxian[1]	Soil carbonates	36.4	111.1	1148	-5.5	-6.7	-4.7	-2.0	-3.3	-3.6	This study
Guliya[2]	Ice Core	35.3	81.5	6200	N/A	-5.3	-2.4	-6.6	-7.4	-7.4	Thompson et al., 1997 (58)
Dunde[3]	Ice Core	38.1	96.2	5325	N/A	-5.4	-3.6	-2.0	-6.9	-0.6	Thompson et al.,1989 (59)
Hulu[4]	Speleothem	31.7	110.4	1900	N/A	-7.8	-5.2	N/A	-2.3	-0.9	Wang et al, 2001 (60)
Dongge[4]	Speleothem	25.3	108.1	680	N/A	-8.3	-7.4	N/A	-3.2	-3.1	Dykoski et al, 2005 (61)
Hulu/Dongge[5]	Speleothem	N/A	N/A					0.3			

LGM-PD/H refers to values from the last glacial maximum (LGM) minus values deterimned for either the present day (PD) or Holocene (H).
Whether the difference presented is between LGM, PD, Late Holocene, or Early Holocene differs between proxy records due to the availability of proxy data for each time period. We elaborate on this point below.
JJA refers to June, July, August average
MA refers to mean annual average
In the case of model output, here values are all the difference between LGM and PD simulations with the high resolution LMDZ model described in this study

[1]Puxian oxygen isotope values are the calculated values of meteoric water (V-SMOW)
[2]In the case of the Guliya ice core record, out of necessity we present the difference between early Holocene (6.8 to 10 ka) to LGM (in this case 18 to 21.1 ka) and we have also included a correction of -1.2‰ for ice-volume change
[3]In the case of the Dunde ice core record, out of necessity we present the difference between late Holocene (6.8 to 10 ka) to LGM (in this case 18 to 21.1 ka) and we have also included a correction of -1.2 ‰ for ice-volume change
[4]In the case of Hulu and Dongge caves, there is not LGM and Late Holocene data for spelothems from individual cave sites so LGM-PG/H values cannot be calculated for each site in isolation
[5]In order to calculate an LGM-H value from speleothem records we have to splice together the Dongge and Hulu records, which introduces uncertainty although they are very similar in absolute values where they overlap.
For speleothem LGM-H comparison we use an average of 18 to 23 ka from the Hulu record to define LGM values (-6.4‰, V-PDB) and 0-1 ka from the Dongge (-7.8‰) record to define H values.
We have also included a correction of -1.2‰ for ice volume change
No temperature component was factored into the Hulu/Dongge LGM-H value of 0.3‰
We note that if a significant temperature component was factored into the speleothem difference then it would result in ^{18}O-depleted isotopic values more similar to our proxy and model results.